# ABSTRACT

Title of Thesis: DEVELOPMENT OF KRYPTON PLANAR LASER INDUCED FLUORESCENCE METHODS FOR THE MEASUREMENT OF HYPERSONIC FLOW CONDITIONS

Chase Standage
Master of Science, 2021
UMD Department of Aerospace Engineering

Advised by: Dr. Kenneth Yu
UMD Department of Aerospace Engineering

Dr. Ashwani Gupta
UMD Department of Mechanical Engineering

Mr. Mike Smith
Arnold Engineering Development Complex

Conventional wind tunnel flow measurement techniques typically involve the use of intrusive sensor systems, such as Pitot-probes and transducers which come in contact with the flow. Intrusive methods become impractical for high Mach number flows, as such methods can cause considerable disruption to the integrity of flow measurements. Therefore, it is desirable to utilize non-intrusive methods in such experiments, especially as hypersonic flow conditions are achieved. Schlieren and shadowgraph imaging methods have been used successfully for decades as a method of non-intrusive flow visualization. However, these methods become obsolete when the path of light is obstructed, which is a common problem when analyzing concave surfaces and complex geometries.

The goal of this project was to develop a scalable krypton planar laser induced fluorescence flow visualization system for use on curved-surface geometries in support of the hypersonic Boundary Layer Transition (BOLT) program. The system was designed to fit multiple wind-tunnel facilities, including the AEDC Tunnel 9 hypersonic test facility and UMD Ludwieg Tube.

In order to design and test the system, the AEDC Mach 3 Calibration wind tunnel was utilized and Kr-PLIF measurements were taken about a 0.50" spherical model and 2" BOLT model. A wide variety of equipment and methods were assessed for their suitability of this project, including 3 cameras and 7 sheet combinations.

A beam from a single-diode Ti-Sapphire laser was amplified, modulated, and shaped in order to create a thin laser-sheet of 0.25-1.0" width and 0.01"-0.025" thickness, frequency of 1 kHz, and pulse width of 40 fs. The flow was seeded with 5% krypton, and tests were conducted at Mach 3.

The results were compared to Schlieren imaging tests conducted onsite in the same Mach 3 wind tunnel. The Kr-PLIF method was moderately successful in finding regions of relatively high flow density, such as boundary layers and leading edges at an angle-of-attack. Additionally, Kr-PLIF was able to make measurements about the curved region of the BOLT model, which was previously unobservable by Schlieren imaging.

# DEVELOPMENT OF KRYPTON PLANAR LASER INDUCED FLUORESCENCE METHODS FOR THE MEASUREMENT OF HYPERSONIC FLOW CONDITIONS

by

Chase Standage

Thesis submitted to the Faculty of the Graduate School of the
University of Maryland, College Park in partial fulfillment
of the requirements for the degree of
Master of Science
2021

Thesis Defence Committee:
Dr. Ashwani Gupta, Co-Chair/Co-Advisor
Dr. Kenneth Yu, Co-Chair/Co-Advisor
Dr. Christopher Cadou, Committee Member
Mike Smith, AEDC Tunnel 9 Advisor

## Acknowledgments

I owe my gratitude to all the people who have made this thesis possible and because of whom my year of graduate education experience has been one that I will take with me indefinitely the future.

First and foremost I'd like to thank my advisor, Dr. Ashwani Gupta for reaching out to me with the invaluable opportunity to work in the challenging, yet incredibly important field of hypersonics. He has been extremely helpful throughout this whole process, and was always available. It has been humbling to work with and learn from such an expert in the field.

I would also like to thank the entire team at the US Air Force AEDC Tunnel 9 facility, all of whom have selflessly lent their time and expertise into making this project possible. Mr. Mike Smith has been invaluable to this research each step of the way and, without him, this thesis would not be possible. Mr. Smith has lent countless hours to assisting me, and provided me with the tools and training necessary to accomplish meaningful work.

I would also like to acknowledge the role of Air Force and U.S. government in providing the funding to make this project possible. Additionally, I owe my gratitude for the U.S. Navy for allowing me to undergo graduate education at the University of Maryland prior to reporting to flight school at NAS Pensacola.

Finally, I owe my deepest thanks to my parents, who have always challenged me to take the harder path, and who have supported me through every step of the way in my education process.

# Table of Contents

List of Figures

# List of Abbreviations

| | |
|---|---|
| AEDC | Aerospace Engineering Development Center |
| APL | Applied Physics Laboratory |
| BOLT | BOundary Layer Transition |
| CARS | Coherent Anti-Stokes Raman Scattering |
| CCD | Charge-Coupled Device |
| CMOS | Complementary Metal-Oxide-Semiconductor |
| FLEET | Femtosecond Laser Electronic Excitation and Tagging |
| HTLT | High-Temperature Ludwieg tube |
| ICCD | Intensified Charge-Coupled Device |
| IR | Infrared |
| IRO | Intensified Relay Optics |
| JHU | Johns Hopkins University |
| KTV | Krypton Tagging Velocimetry |
| LIDT | Laser-Induced Damage Threshold |
| Nd:YAG | Neodymium-doped Yttrium-Aluminum-Garnet |
| NIST | National Institute of Standards and Technology |
| OPA | Optical-Parametric Amplifier |
| OPA | Optical-Parametric Oscillator |
| PIV | Particle Image Velocimetry |
| PLIF | Planar Laser Induced Fluorescence |
| UMD | University of Maryland |
| USAF | United States Air Force |
| USN | United States Navy |
| USNA | United States Naval Academy |
| UV | Ultraviolet |
| UVFS | UV Fused Silica |

# List of Symbols

| | |
|---|---|
| $\alpha$ | angle-of-attack |
| $A_{21}$ | Einstein coefficient for transition |
| c | speed of light |
| C | calibration coefficient |
| d | collimation distance between optics |
| f | focal length |
| h | Planck constant |
| $\gamma$ | wavelength |
| l | sheet length |
| m | magnification |
| $M_\infty$ | freestream Mach number |
| n | Kr number density |
| $\rho$ | density |
| $\rho_\infty$ | freestream density |
| Re | Reynolds number |
| $\sigma_0$ | self-quenching cross section |
| S | fluorescence signal |

# Chapter 1: Introduction

## 1.1 The Need for Hypersonic Testing and Evaluation

Hypersonic systems represent a central part of the next generation of military aviation technology and strategy. A country that can field such systems will have a significant advantage in the next major conflict. In contrast to traditional ballistic missiles, these systems may be highly capable of penetrating air defenses and allowing for first-strike capability. Therefore, there is an intense interest by the United States to research and develop hypersonic flight technology, vehicles, and testing methods. As the major world powers invest into the development of hypersonic flight vehicles and weapon systems, the need for accurate testing methods for the hypersonic regime has become more important than ever. Numerical and analytic models of the hypersonic regime can vary greatly in accuracy, and so physical tests are one of the best ways to get fast and accurate information. However, real world flight test of experimental vehicles can be extremely costly, with up to millions of dollars potentially being invested for a single flight test. Therefore, the industry has leaned heavily on the use of wind-tunnel testing in order to gather as much data as possible in place of costly flight tests, and to assist in the validation of simulation models.

The U.S. Air Force's Arnold Engineering Development Complex (AEDC), co-located in Tennessee and Maryland, has focused on the test and evaluation of hypersonic flight vehicles for half a century. The AEDC Tunnel 9 facility, located in White Oak, MD, is one of the nation's premier hypersonic testing facilities, with a wind tunnel capable of routinely producing flight conditions of up to Mach 18. Apart from conducting tests for commercial and military clients, the Tunnel 9 facility has also been a pioneer in the design and development of unique testing methods for hypersonic conditions. Many of these methods have gone on to be commonplace in the larger hypersonic testing community.

The hypersonic flight regime is generally considered to begin above Mach 5, where the dissociation of air begins and extremely high heat loads exist. Traditional models governing supersonic flight begin to break down, leading to the rise of increasingly unpredictable behavior as the Mach number is increased. For example, certain phenomena like thin shock layers, high viscous interactions, and a thick entropy layer lead to pronounced boundary layers that behave significantly different from those in lower Mach number flight conditions. In order to reinforce models that seek to accurately simulate such behavior, real world data to which the models can be compared is needed.

In the hypersonic regime, it is more important than ever to utilize *non-intrusive* methods of measurement, as the change in flow conditions due to intrusive probes can entirely alter and ruin the results of a test. This has led to the development of a wide variety of techniques that utilize light, particularly lasers, to make specific measurements. These methods include Femtosecond Laser Electronic Excitation and

Tagging (FLEET) [1], Particle Image Velocimetry (PIV) [3], Coherent anti-Stokes Raman scattering (CARS) [6], and Planar Laser Induced Fluorescence (PLIF). Additionally, Schlieren and shadowgraph methods have been performed for decades in order to visualize hypersonic shock/expansion waves, turbulence, and other phenomena. The development of PLIF, as an aid to Schlieren/shadograph methods, is the focus of this research.

## 1.2 BOLT Program

A secondary objective for this research into Kr-PLIF is to support the multi-entity BOLT (BOundary Layer Transition) program. The BOLT program is a collaboration between the U.S. Air Force Research Laboratory's Aerospace Systems Directorate and AEDC, NASA Langley, the University of Minnesota, Purdue University, Texas AM University, CUBRC, Australia"s Defence Science and Technology Group, the German Aerospace Center (DLR), VirtusAero, Johns Hopkins Applied Physics Laboratory (APL), and the University of Maryland.

The program seeks to gain a deeper understanding of hypersonic boundary layer transition, and uses a novel test-model to do so. The project began in 2017 with computer simulation testing, as shown by Figure 1.1 and soon transitioned to wind tunnel testing with a highly instrumented model, as shown by Figure 1.2. A full-scale Mach 5-7 flight test of the BOLT Vehicle on-board a sounding rocket is currently planned for the near future (Figure 1.3).

As the program is focused on boundary layer transition, testing methods that can observe flow conditions close to the curved surface of the model are needed. Conventionally, Schlieren imaging could be used to view just above the surface of a flat model, but in the case of BOLT, the curved surface gradient is unable to be examined by Schlieren or other conventional optical methods. Therefore, it could be advantageous for the program to utilize PLIF as a method to make measurements about this otherwise obscured region.

[2]

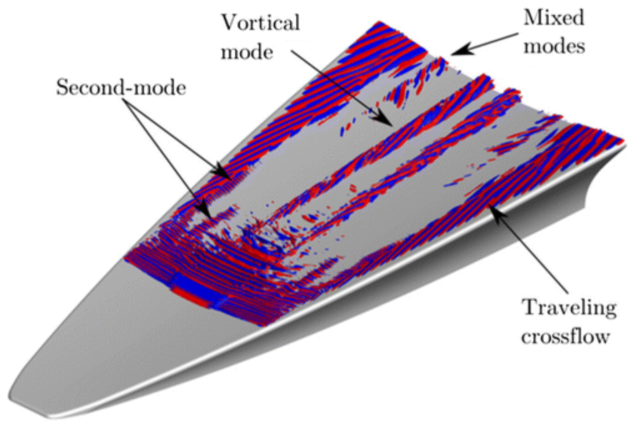


Figure 1.1: BOLT Boundary Layer Transition Simulation

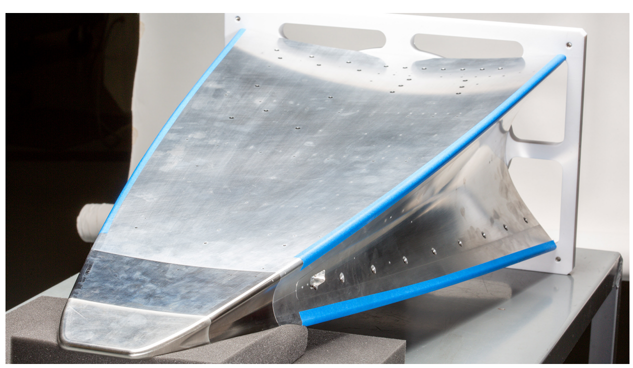

Figure 1.2: Instrumented BOLT Wind Tunnel Model

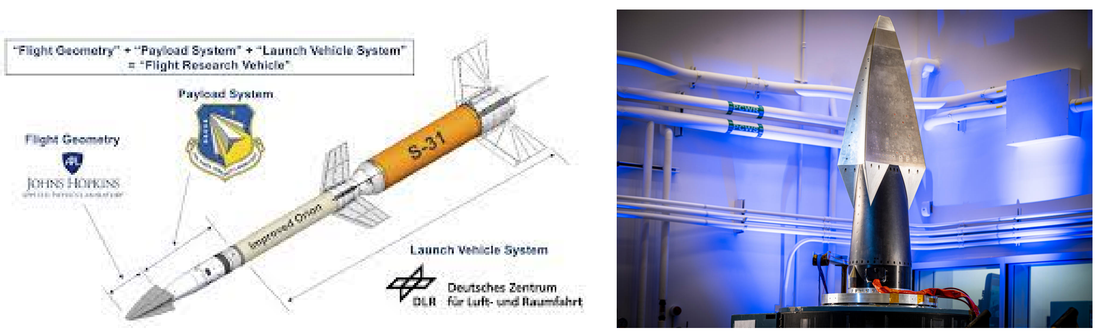


Figure 1.3: BOLT Model onboard sounding rocket (top)

## 1.3 Overview of Planar Laser Induced Fluorescence (PLIF)

PLIF is an established method of measuring the relative density of a region within a flow through the excitation of a gas by a thin laser sheet. PLIF involves the excitation of a gas within the flow of interest and the measurement/recording of photons subsequently emitted from the excited gas as it drops down to a lower energy state. This measurement of emitted photons can be then correlated to the relative density of the flow at the region of measurement. This region is defined by the dimensions of the laser sheet by which the gas is excited. PLIF can also be used to visualize shock and boundary layer formation and behavior, similar to Schlieren imaging. However, PLIF has an advantage over Schlieren imaging in that it can be used to analyze a the flow near a curved surface, which would otherwise obstruct the pathway of light that is imaged via the Schlieren method. Therefore, for certain models, PLIF can theoretically take data from regions which are otherwise obscured to conventional optical methods.

PLIF requires that the flow being analyzed contains molecular particles that have the capability to be excited by a laser, thereby resulting in fluorescence. This means that energy state of the molecules are able to be excited to a higher energy level than the ground state by the absorbance of light. Following this excitation, the molecules are able to return to the original ground state through the release of photons of longer wavelength of than the incident photons. In the case of excitation by UV light, the corresponding photon release is typically in the visible light range, and therefore observable by imaging equipment.

In the past, PLIF measurements have been accomplished in flames by the excitation of combustion bi-products such as $CH_2O$, OH, and NO by a Nd:YAG or Ti-Sapphire laser and an OPO/OPA. An example of this is depicted by Figure 1.5. The application of PLIF for high-speed wind tunnel applications is a rising field, and has been examined in a very limited manner. [6]

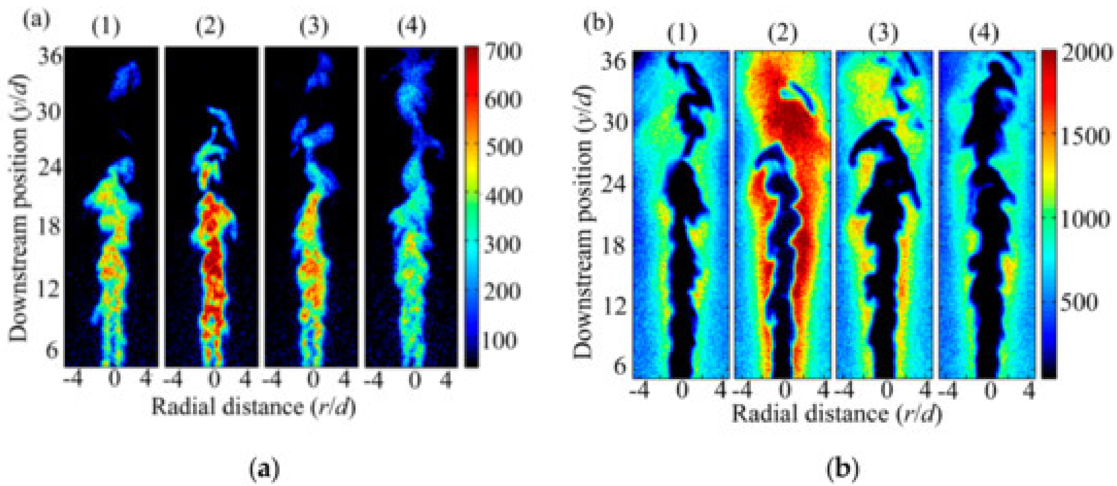


Figure 1.4: (a) $CH_2O$-PLIF instantaneous images and (b) OH-PLIF instantaneous images [7]

The goal of this research was to develop hypersonic flow visualization methods via planar laser induced fluorescence of krypton gas by a Ti-Sapphire femtosecond laser. The krypton was chosen due to its relative inertness, which allows it to be used in $N_2$ based flows without disruption to the system. The development is being conducted with the ultimate goal to use the system at the AEDC Tunnel 9 facility and the University of Maryland's high-temperature Ludwieg tube (HTLT). As stated earlier, a primary advantage of PLIF over Schlieren imaging is that it allows measurements to be taken right down to the surface of curved geometries, which would otherwise obscure the free passage of light needed to conduct Schlieren imaging. The BOLT model is an example of one such geometry where Schlieren images cannot be taken down to the surface. In the case of BOLT, the primary focus of the experiment happens to be at the surface of the model (where boundary layer transition occurs), so the development of Kr-PLIF in hypersonic conditions is valuable as an experimental data supplement to the BOLT program.

## 1.4 Development of a PLIF System: Component Overview

PLIF systems principally require four main components:

1. Excitable Gas and Delivery System
2. High Power Laser
3. Sheet Forming Optics
4. Intensified Camera

A simplified PLIF system is shown by Figure 1.5. Each of the four main components are described in the following sections.

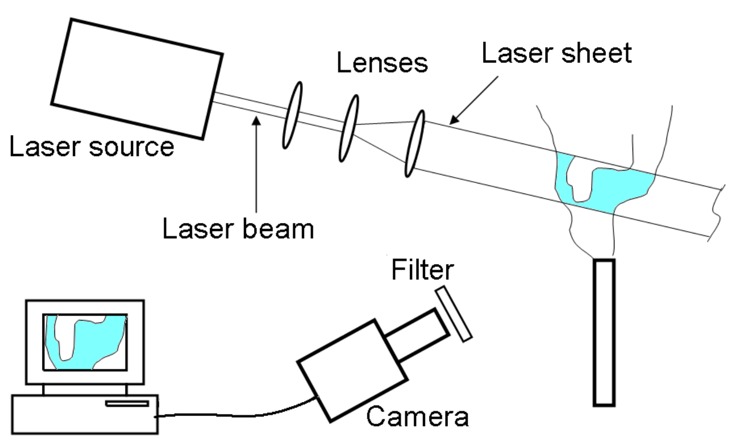


Figure 1.5: Simplified PLIF System Setup.

### 1.4.1 Seeding Gas and Process

In order for measurements of PLIF to be accomplished, there must be some molecular species in the flow that is able to be excited by a laser in order to induce a release of visible photons (fluorescence). Fluorescence is the emission of light by a substance following the absorbance of light or other electromagnetic radiation. In most cases, the photons being absorbed by the substance are of a higher energy, and therefore shorter wavelength, than the photons which are emitted. For this research, the two-photon fluorescence of krypton is accomplished with an absorbed light wavelength of 212.5 nm and a broadband of emitted wavelengths between 740 and 820 nm. The two most prominent of these emitted wavelengths are 760 nm and 810 nm, with 760 nm being the focus of this research. This is further discussed in Section 1.4.1.1.

As stated before, PLIF has been extensively accomplished in the past using compounds such as nitric-oxide (NO), formaldehyde ($CH_2O$), and hydroxyl (OH) radicals. The advantage performing PLIF with these gas particles is that they are naturally occurring in their respective flows; nitric-oxide is a naturally present-species in air-based hyper-velocity flows (particularly above Mach 6), and formaldehyde/hyrdroxyl radicals are commonly present in hydrocarbon-fueled combustion systems. However, nitric-oxide, and many other hypersonic flow radicals, are highly corrosive and potentially destructive for test systems. Optics, models, and other system components have significantly degraded lifetimes when exposed to these destructive molecules. The degradation can be to the point where the experimental setup only lasts for one tunnel run. While this can be acceptable under some circumstances, where the value of the data overshadows the cost of the experimental setup, this is not often the case. This is one of the primary reasons for the use of pure $N_2$ in hyper-velocity flow systems. Therefore, it is desired to perform PLIF using a seeded gas that gives measurable fluorescence *without* disrupting flow characteristics or causing damage to the experimental setup. This is the advantage of using krypton (Kr).

While Kr is a heavy gas, with an atomic weight of 83.798u and atomic number of 36, it does not have an appreciable effect on flow conditions or behavior when introduced in low concentrations ($<$10% for Mach 3, $<$1% for Mach 18). Additionally, it is one of the six naturally occurring noble gases, which means it is relatively non-reactive under low-pressure conditions. [5] While xenon, and argon are more naturally abundant, the fluorescence of krytpon is well characterized and determined to be more energetic at its peak levels than the former noble gases.

#### 1.4.1.1 Spectra Measurement

In order to decide upon an appropriate camera filter to be used for the imaging of krypton PLIF, the emission spectra of fluoresced krypton was assessed. This was compared with the spectra that was expected from literature.

According to literature, the most energetic two-photon releases from krypton occur via excitement by light with a wavelength of 212.5 and 214.7 nm. Generally, a stronger series of emissions occurs from an exciting by 212.5 nm. This excitation results in the emission of photons among a broad spectrum range between 740 and 820 nm. However, the most prominent of these emissions occurs at 760 and 810 nm, as shown by Figure 1.6. [9]

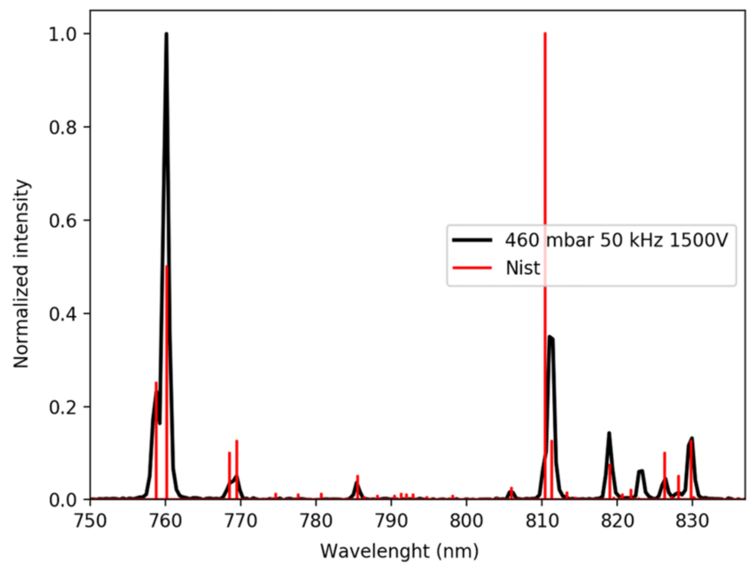


Figure 1.6: Two-photon emission spectra of krypton excited by a 1500V power source at 50 kHz. NIST database results also shown [9].

The krypton state-transition diagram for the 212.5 nm excitation is shown by Figure 1.7. 212.5 nm stimulates Kr from a resting state of $4p^6 1s_0$ to an excited state of $5p[3/2]_2$. The excited Kr then releases photons from $5s[3/2]_1$ and $5s[3/2]_2$ in order to return to the unexcited resting state. [19] These photon releases result in measurable fluorescence. The number of photon releases, and therefore the magnitude of fluorescence intensity, is dependent on both the gas density and laser power. The analytic relationship between the signal of fluorescence and Kr density is given by 1.1:

$$S = C \frac{A_{21}}{A_{21} + \sigma_0 n v} n \tag{1.1}$$

where S is the fluorescence signal, n is the Kr number density, $A_{21}$ is the Einstein coefficient for the transition, $\sigma_0$ is the self-quenching cross-section, v is the frequency of the released photon, and C is the calibration coefficient.

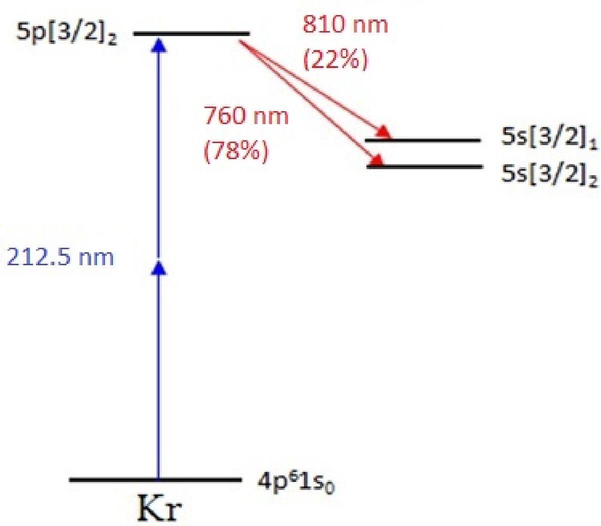


Figure 1.7: 212.5 nm to 760/810 nm state-transition diagram for krypton gas.

In order to verify the data from literature and the National Institute of Standards and Technology (NIST) database, an early analysis of the krypton emission spectrum was made using a Acton Research Corporation SpectraPro-2500i spectrometer, enclosed krypton sample at 10 torr, and laser at approximately 212.5 nm. The results from this evaluation are shown by Figure 1.8.

### 1.4.2 Tunable High Power Laser

In order to excite the krypton gas, a laser system is required that can produce the desired wavelength as well as output enough power such that the krypton fluorescence is measurable. Additionally, due to the high-speed nature of the flows that this Kr-PLIF system is being designed to analyze, the laser must have a sufficiently

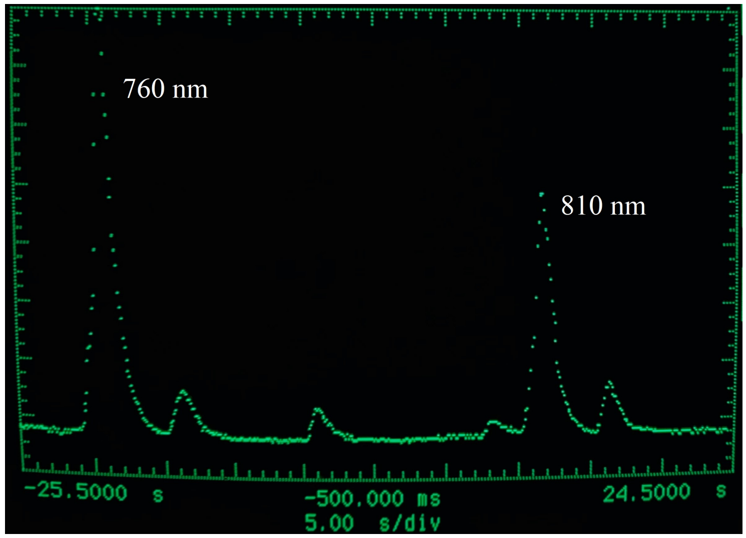


Figure 1.8: Experimental two-photon emission spectra of krypton, as captured by spectrometer.

short pulse-width. As flow speeds are increased, it becomes increasingly important to have a shorter pulse width, in order to prevent an image from blurring as an excited molecule moves through the camera frame during the duration of the pulse width. For example, at Mach 18, the flow velocity is about 2 mm/ms, which would result in significant image blur for the long pulse width of a continuous wave laser.

Therefore, the requirements outlined for this system are that the laser must produce an output at 212.5 nm with a short pulse width on the order of femtoseconds ($10^{-15}s$). In the past, PLIF setups have utilized nanosecond ($10^{-9}s$) lasers, which reduce the laser energy output requirements by a factor of about 100 [12]. However, nanosecond lasers typically have a lower repetition rate, on the order of 10 Hz, which does not provide a very large sample set of data for tests that last on the order of just seconds. In contrast, the femtosecond laser being used has a repetition rate of 1 kHz, which provides a much larger sample size, especially for flows lasting less than one second (as is often the case in shock tubes).

The process used to produce the 212.5 nm laser beam is discussed in Section 2.1.4

### 1.4.3 Sheet Forming Optics

In order to acquire measurements about a whole region of interest, rather than just a thin line, the laser beam must be formed into a sheet. This sheet must be of sufficient width in one direction to interrogate the entire desired region of interest, while also be of sufficient thinness to maximize the energy-density, and therefore maximize the level of excitement from the krypton gas.

A variety of sheet forming methods and wide combination of optics were tested in the development of the Kr-PLIF system. The specifics of each setup are discussed in Section 2.2.2.

### 1.4.4 Image Capture

Due to the high velocity of the flow to be tested, a high-speed camera is desired in order to capture the maximum amount of laser-pulses/krypton-fluorescence cycles. Due to the anticipated weak signal of krypton fluorescence, the camera must also be either internally-intensified or compatible with an external intensifier.

Additionally, the camera should be operated in a gate-mode, which allows each pulse to be captured discreetly while minimizing noise from background sources. Due to the weak signal of fluorescence, elimination of background noise is essential for the analysis of signal-results, and is one of the key-considerations when post-processing the PLIF data.

### 1.4.5 Post Processing

Following image capture and extraction, post-processing software can be used to perform background reductions, smoothing functions, and calculations in order to measure the relative density of the flow within the region of interest. The LaVision Davis software is described in greater detail in Section 2.7.

## 1.5 Schlieren Imaging

In order to provide a reference baseline to which the Mach 3 Kr-PLIF results could be compared, Schlieren imaging was also conducted about the sphere and BOLT models. Schlieren is a visual process that is used to photograph the flow of fluids of varying density. It is a highly valuable and non-invasive tool in visualizing shock formation in supersonic conditions.

Schlieren utilizes a collimated light sources shining from behind a target object. The collimated light beam is refracted by density gradients in the fluid, which can be directly visualized by a camera. Typically, the light is focused with a converging mirror/lens, and a knife edge is placed at the focal point of the light. This results in lighter and darker shades which correspond to positive and negative fluid density gradients in the direction normal to the knife edge. The knife edge of a Schlieren system results in the *first* derivative of the density gradients to be observed by the camera. [10]

# Chapter 2: Experimental Setup

## 2.1 Laser Setup

There are three main components used to produce the laser beam at 212.5 nm: the Ti-Sapphire laser, optical-parametric amplifier (OPA), and optical-parametric oscillator (OPO).

### 2.1.1 Solstice Ace Ti-Sapphire Laser

The Solstice Ace Ti-Sapphire Laser is a tunable system that produces >7W of power at 1 kHz within the range of 780–820 nm. The laser can produce a pulse-width between 35-120 fs. First invented and used at the MIT Lincoln Laboratory in 1982, Ti-Sapphire lasers use a crystal sapphire $Al_2O_3$ lasing medium which is doped with $Ti^{3+}$ ions. One of the primary advantages of a Ti-Sapphire laser is its ability to produce ultrashort pulses in the femtosecond range at very high repetition rates, as opposed to the much lower repetition rates of nanosecond lasers, such as Nd:YAG lasers commonly used in the past. While carrying less energy per pulse, this allows femtosecond lasers to increase the data sampling rate by 1-2 orders of magnitude. This is advantageous in extremely high speed flows, such as the Mach 7-18 range of the Tunnel 9 facility, which may only last on the order of a couple seconds.

### 2.1.2 Spectra Physics Topas Prime Optical-Parametric Amplifier (OPA)

An OPA is a laser-light source which emits light of varying wavelengths following an optical parametric amplification process. The OPA takes in a pump beam from the Ti-Sapphire laser and sum-frequency mixes it with an idler beam to generate a signal beam. The OPA then amplifies the resultant signal beam. The final output of the OPA then is the amplified signal beam and the idler beam. These beams are then used as inputs into the OPO.

The Spectra Physics Topas Prime OPA is a femtosecond capable amplifier that can take up to 5 mJ of input energy (pump) from wavelengths between 770-830 nm. The exterior and interior are shown by Figures 2.1 and 2.2 for reference.


Figure 2.1: Spectra Physics TOPAS Prime OPA (Exterior)

### 2.1.3 NirUVis Optical-Parametric Oscillator (OPO)

Similar to the OPA, the OPO takes in a pump beam to generate a new set of wavelengths through a sum-frequency mixing process. However, it does this by

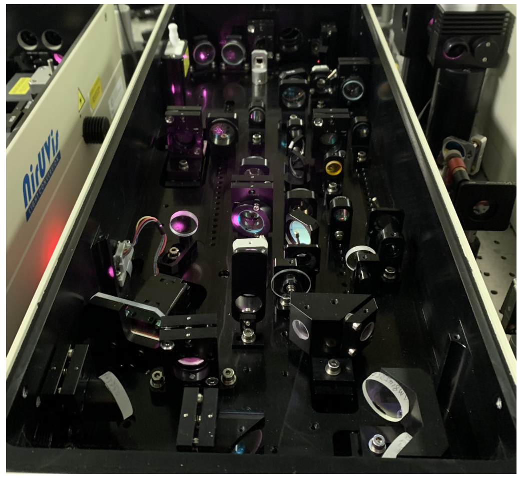

Figure 2.2: Spectra Physics TOPAS Prime OPA (Interior)

means of second-order nonlinear optical interaction within an optical cavity, which contains a series of optical resonators and crystals. The primary output of the OPO is a beam of the desired wavelength, 212.5 nm, as well as residual wavelengths (810, 576, 288 nm) from prior mixing and doubling processes.

The NirUVis is an add-on frequency mixing OPO for the TOPAS Prime OPA. The advantage of the NirUVis system is its designed compatibility with the TOPAS Prime OPA, as well as its ability to be automatically controlled and calibrated from a master computer. It offers laser tuning from 189 nm to 20 $\mu$m and has an estimated conversion efficiency of $> 25\%$ at 212.5 nm.

### 2.1.4 Wavelength Generation

In order to generate the 212.5 nm beam, a series of sum-frequency mixing and doubling processes occur with the OPA and OPO. First, the 810 nm ouput from the Ti-Sapphire laser and the 2029 nm ouput from the OPA undergo sum-mixing to produce 576 nm, as described by Equation 2.1.

$$\frac{1}{\lambda_{new}} = \frac{1}{\lambda_1} + \frac{1}{\lambda_2} \tag{2.1}$$

Sum-mixing is a second order nonlinear process based on the annihilation of two input photons with distinct angular frequencies, and the subsequent generation of an output photon that conserves the total incident angular frequency. This process is governed by the conservation of energy. [18]

Next, the 576 nm beam is frequency-doubled through a doubling-crystal in order to produce 288 nm, as described by Equation 2.2.

$$\lambda_{new} = \frac{1}{2}\lambda_{old} \tag{2.2}$$

Frequency-doubling, or second-harmonic generation is a nonlinear optical two-photon process where the photons, each with the same input frequency, interact with a material and are combined, resulting in the generation of a new photon that carries twice the energy of the initial photons. This is explained by Planck's Equation (2.3):

$$E = hf = \frac{hc}{\gamma} \tag{2.3}$$

where E is the photon energy, h is Planck's constant, h is the frequency, h is the speed of light, and $\gamma$ is the wavelength.

Finally, the 288 nm beam undergoes sum-mixing by Equation 2.1 with a beam of 810 nm from the Ti-Sapphire laser in order to produce a beam at approximately 212.5 nm. This 212.5 nm beam still carries residuals of 288, 576, and 810 nm which could be seen by an unfiltered intensified camera. However, most of the residual energy is dumped by the series of UV fused-silica mirrors/prisms.

### 2.1.5 Laser Tuning

The laser was initially tuned to the desired 212.5 nm wavelength by using an Ocean Optics QE Pro High Performance Spectrometer. The spectrometer allows a beam to be input via a fiber optic cable, and can measure wavelengths between 200-900 nm. However, this device has an accuracy band of +/- 0.5 nm, and so a more accurate method was need to precisely tune to 212.5.

The laser was more precisely tuned to the desired wavelength by the following method. A vacuum cell was pumped with 100% Kr gas to 1 atm. The cell had windows appropriate for both the passage of the laser sheet, and the recording of fluorescence with an intensified camera. The laser was tuned such that a maximum signal of fluorescence was obtained from the krypton within the cell. This was done by making 0.05 nm changes to the laser software settings, and adjusting for timing delay changes with the final delay stage in the OPO.

## 2.2 Optics

### 2.2.1 Mirrors

The 0.25" diameter beam was directed towards the tunnel test-section by a series of four mirrors. Each UV fused-silica mirror was one inch wide, and rated for 213 nm with a reflectance of 95%. The first mirror results in a power loss of about 0.3 mW, partially attributed to the transmission of residual infrared (IR) wavelengths from the laser mixing process. While resulting in a power loss, this transmission through the mirror removes the unwanted IR residuals from the UV beam. Each successive mirror reflection thereafter resulted in a power loss of about 0.1 mW, for a total power loss due to mirrors of about 0.6 mW. The path of the beam from the laser output to the tunnel test-section is shown by Figure 2.3.

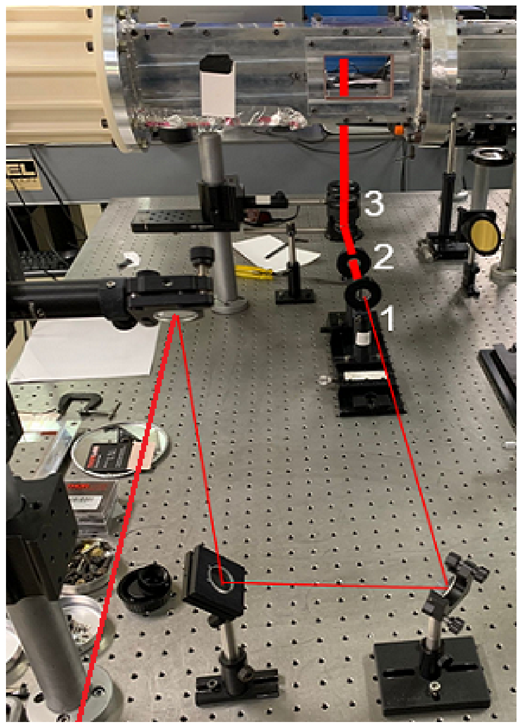


Figure 2.3: Example of the beam path as it travels from the first mirror, through the sheet-forming optics, and into the tunnel. The labeled optics are (1) -50 mm cylindrical plano-concave lens, (2) 200 mm cylindrical plano-convex lens, (3) 250 mm cylindrical plano-convex focusing lens.

#### 2.2.1.1 Alternate: Prism

Near the end of the research, it was discovered that the Yt-As coating on the surface of the UV fused-silica mirrors was severely damaged through nano-cracking, leading to a near total loss in laser power following the damaged mirror. It is believed that the damage was due to the femtosecond pulse-width of the laser. As the pulse width decreases for a laser, the power density increases, and the dielectric coating on mirrors tends to become excited and displaced. This nano-cracking effect is shown by Figure 2.4, and the relationship between laser pulse-width and mirror damage threshold is shown by Figure 2.5. [14]

Figure 2.4: [15]

### 2.2.2 Sheet Forming Optics

A variety of laser sheet formations were evaluated. The creation of each specific sheet profile is described in the following subsections. For this discussion, the sheets are said to have width in the x-direction, and thickness in the y-direction, where "x" and "y" are shown by Figure 2.6.

An example of an x = 0.50" x y = 0.025" collimated sheet is shown by Figure

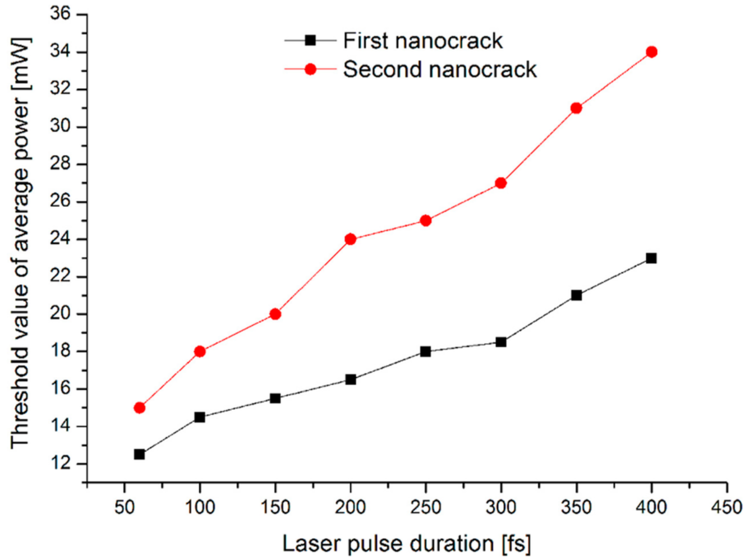


Figure 2.5: Average Laser Induced Damage Threshold vs Laser Pulse Duration (Width). [14]

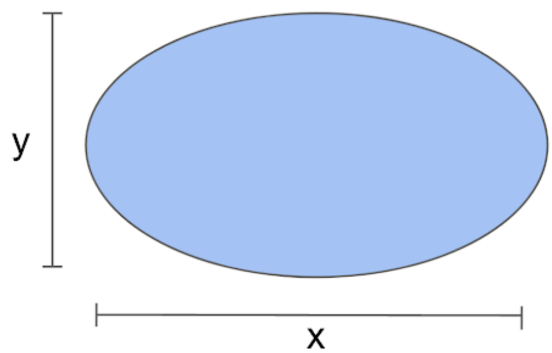


Figure 2.6: Sheet Dimensions Diagram

2.7.

The expansion ratio produced by a pair of cylindrical plano-concave and cylindrical plano-convex lenses is given by Equation 2.4,

$$m = \left( \frac{f_{convex}}{f_{concave}} \right) \tag{2.4}$$

Where m is magnification, $f_{convex}$ is the absolute value of the focal length of the cylindrical plano-convex lens, and $f_{concave}$ is the absolute value of the focal length

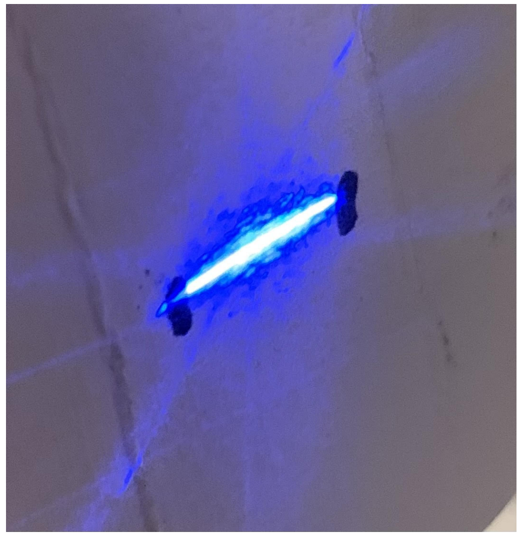

Figure 2.7: 0.5" x 0.025" Laser Sheet Example.

of the cylindrical plano-concave lens.

The distance required between optics in order to produce a collimated sheet is conventionally given by Equation 2.5,

$$d = f_{concave} + f_{convex} \tag{2.5}$$

However, Equation 2.5 is appropriate only if the wavelength of light being transmitted is equivalent to the manufacturer specified optic rating. In this case, the optic rating for the cylindrical lenses is given as 580 nm. The corrected distance can be *approximated* by Equation 2.6,

$$d_{corrected} = \frac{\lambda}{\lambda_{spec}} \left( f_{concave} + f_{convex} \right) \tag{2.6}$$

where $\lambda$ is the laser wavelength (212.5 nm) and $\lambda$ is the optic rating (580 nm). However, this only applies to the assumption of a thin lens. Because of the relatively thick nature of the plano-convex lens, Gullstrand's Equation must be utilized instead:

$$d_{Gullstrand} = \frac{f_{concave} f_{convex}}{f_{concave} + f_{convex} - \frac{t}{n}} \tag{2.7}$$

where $d_{Gullstrand}$ is the corrected distance between lenses, t is the thickness of the lenses, and n is the refractive index of the lenses. This gives a close approximation of the separation needed between the lenses for collimation, and the exact collimation of the sheet can be further tuned by hand.

Using this process, a variety of sheet combinations between 0.25" and 1.0" in length, 0.025" and 0.25" in thickness, and collimated or focused were formed and tested. In all, 10 different sheet combinations were evaluated in preliminary testing.

## 2.3 Krypton Gas

### 2.3.1 Concentration

$Kr/N_2$ mixtures can be purchased in any concentration. 100% Kr gas was used for initial laser fluorescence testing, but it is not practical to seed the tunnel directly with 100% Kr, as the exact total concentration of Krypton amongst other tunnel gases is then just a rough estimate based on the approximated volume of Kr added to an approximate volume of total gas.

Therefore, it was desired to purchase a known $Kr/N_2$ mixture. Due to the relatively heavy atomic weight of Kr (83.798 u) compared to $N_2$ (14.01 u), it is desired to minimize the concentration of Krypton in order to not appreciably alter the density and behavior of the flow being studied from what would be encountered in a 100% $N_2$ flow.

In order to determine a suitable Kr/$N_2$ concentration, which is as minimal as possible but still high enough to produce a suitable fluorescence signal, a vacuum cell was filled with 100% Kr and then pumped down to fractions of 1 atm in order to simulate lower concentrations of Kr. For example, to simulate a 5% Kr, 95%$N_2$ mixture, the cell was filled with 100% Kr at 1 atm, and then pumped down to 0.05 atm. The limitation of this method is that there is still trace amounts of oxygen in this cell, particularly at lower pressures where more oxygen can leak in, which can lead to quenching.

As shown by Figure 2.8, the signal of fluorescence was very strong at 100% Kr, with a 10:1 average signal-to-noise ratio. As the concentration was brought down to 5%, the signal was still suitable, with a 4:1 average signal-to-noise ratio. However, as the concentration was decreased to 3%, the signal-to-noise ratio decreased to an average of 1.5:1, which was not acceptable for Kr PLIF. It was also noted that the fluorescence signal decreased slightly (by about 5%/inch, as viewed from top to bottom) as the laser sheet passed through the Kr gas. This is due to the absorbance of the laser power by the Kr molecules as they are excited to a higher energy level. While not significant on a small scale, this could lead to large reductions in fluorescence if the laser sheet has to pass through a large region of Krypton gas before reaching the region of interest, which may be encountered in larger test sections.

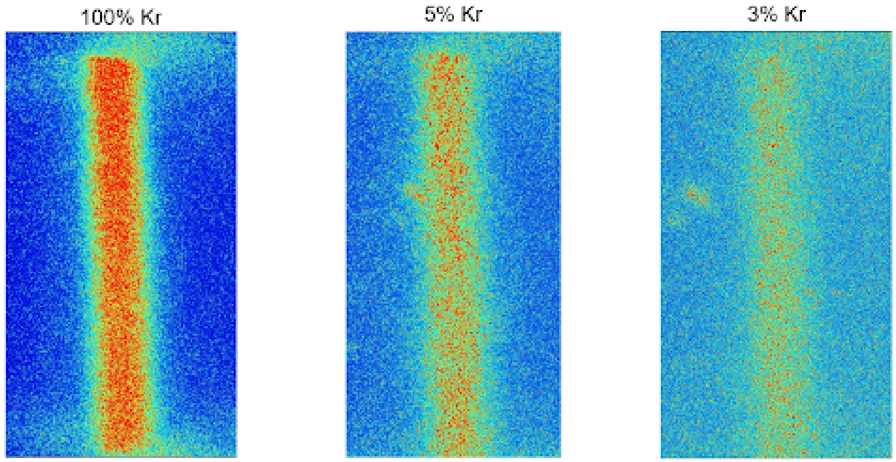


Figure 2.8: Effect of Kr concentration on fluorescence

## 2.4 Mach 3 Calibration Tunnel

The Mach 3 AEDC Calibration Tunnel is an indraft supersonic wind tunnel, driven by a large vacuum tank with a converging-diverging nozzle attached to it. To start the tunnel, a valve is cycled downstream of the nozzle throat. The regular effective reservoir is the ambient laboratory air and so the freestream conditions are fixed at about 1 atm.

The test section, shown by Figure 2.9 has three separate stations which each have four locations to insert windows, aluminum blocks, valves, etc.. This allows more than one experiment to be setup at a time using the calibration tunnel, as was the case during this project. The test section has a square cross section of about 2.5" in each dimension, which allows for a model with a frontal area of about 1-in$^2$ to be used without unstarting the flow. The exact maximum frontal area is dependent on the geometrical nature of the model.

For each run, the tunnel was pumped down to 20 Torr. The valve was opened

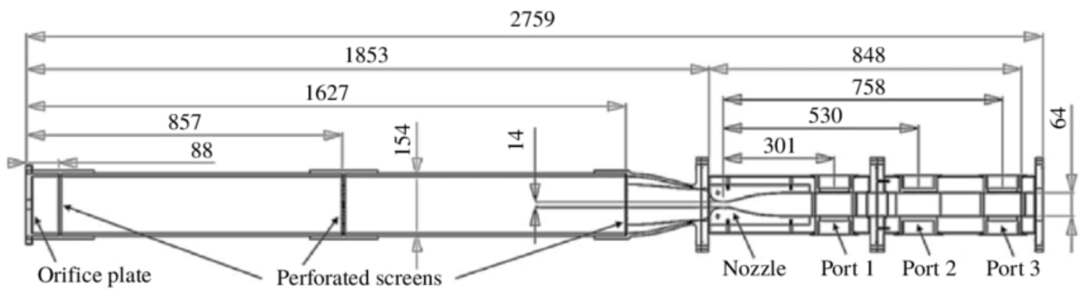


Figure 2.9: Mach 3 Calibration Tunnel: Test Section Diagram

until a cutoff point of 50 Torr. This fully drained the reservoir bag without sucking the bag into the test-section inlet, and allowed for about 5 seconds of flow in each tunnel run. Additionally, the Reynolds number could be manually adjusted by changing the orifice plate diameter. This relationship is shown by Figure 2.10.

| Experiment | $M_\infty$ (-) | $P_\infty$ (Pa) | $T_\infty$ (K) | $\rho_\infty$ (kg/m$^3$) | $\mathrm{Re}_\infty^{unit}$ (1/m) | $\mathrm{Re}_\Theta$ (-) | $U_\infty$ (mm/µs) | $\tau_m$ (µs) | $x_m$ (mm) |
|---|---|---|---|---|---|---|---|---|---|
| Underexpanded Jet | 5.00 | 340 | 49.3 | 0.024 | 79.7e6 | - | 0.714 | 4.5 | 3.2 |
| Mach 3 AEDC Calibration Tunnel - 12.7 mm OP | 2.75 | 550 | 118 | 0.016 | 1.26e6 | 800 | 0.614 | 7.6 | 4.7 |
| Mach 3 AEDC Calibration Tunnel - 19.1 mm OP | 2.77 | 1010 | 118 | 0.030 | 2.30e6 | 1400 | 0.612 | 4.1 | 2.5 |
| Mach 3 AEDC Calibration Tunnel - 25.4 mm OP | 2.73 | 1825 | 118 | 0.053 | 4.16e6 | 2400 | 0.611 | 2.1 | 1.4 |

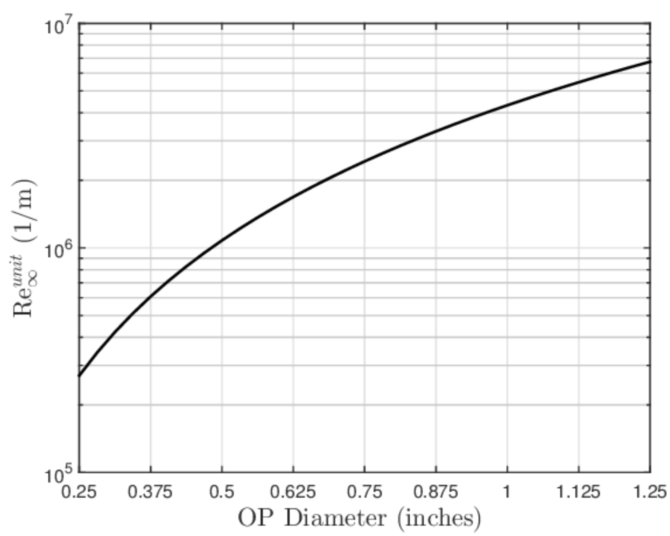


Figure 2.10: Mach 3 Calibration Tunnel: Reynolds Number vs Orifice Diameter

For the tests conducted in this research, a 19.1 mm (0.75") opening was used, resulting in $\mathrm{Re}_\infty \approx 2.30 \times 10^6$ (1/m) and $\mathrm{M}_\infty \approx 2.77$. This also results in $\rho_\infty \approx$

0.030 kg/m$^3$, or 0.025 atm.

The initial and final 500 ms of each run are dominated by unsteadiness and shock reflections as the flow and shocks develop within the test section and about the test article. The development of supersonic flow and shock structures within the tunnel is known as starting. Conversely, the reverse process is known as unstarting. Unstarts commonly occur when there is a rapid change in mass flow rate through a supersonic duct. This change in mass flow rate is experienced during the initial and final phases of each tunnel run. Therefore, data was mainly analyzed from portions of each test after the initial second and before the final second of flow. Through Schlieren imaging, steady supersonic flow could be observed during the 2-3 seconds between these extremes.

### 2.4.1 Seeding Method

An 8-ft long, 1-ft diameter cylindrical PVC pipe was attached to the inlet end of the tunnel test-section, before the nozzle. On the free end of the pipe, an 85 gallon, 7mm thick, drum-shaped plastic bag was attached to store gas for each tunnel run. This allows for a maximum gas capacity of about 36 ft$^3$. In order to prevent the bag from being ingested into the inlet pipe, a plastic frame was constructed to give rigidity to the bag section. Gas was directly injected into the test section before each run through a line connected to a pressurized tank of 95%$N_2$/5%Kr mixture. The setup is shown by Figure 2.11.

The system took approximately three minutes to fully fill to 1 atm with the gas mixture before each tunnel run. The 36 $ft^3$ of gas allows for a total run time of about 5 seconds.

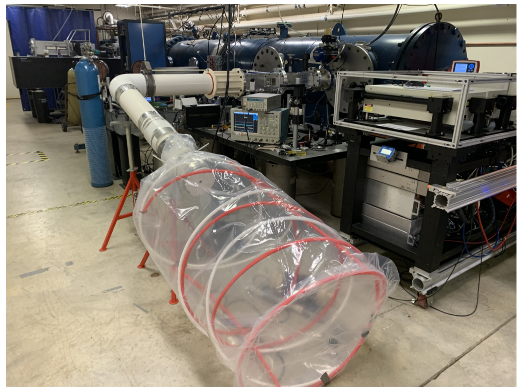

Figure 2.11: Gas containment and seeding system.

### 2.4.2 Pricing

The 5% Kr, 95% $N_2$ mixture was purchased in pressurized 256 $ft^3$ bottles for a price of $800. Each bottle provided enough gas for about 15 runs in the Mach 3 calibration tunnel. This results in an average cost of about $55/run.

## 2.5 Models

### 2.5.1 Stainless Steel Sphere

A 0.5" diameter stainless-steel sphere was mounted to a sting and positioned in the center of the tunnel test section. The sphere was chosen for initial testing due to the abundance of prior shock data provided via Schlieren imaging to which the results of the Kr-PLIF could be compared.

Examples of the shock formation at Mach 1.2 about a spherical object are given

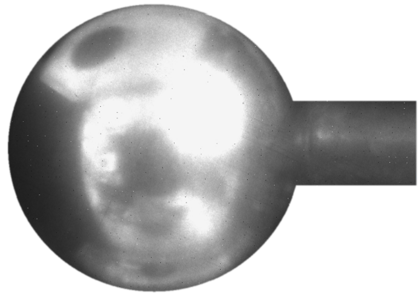

Figure 2.12: 0.5" Mounted Sphere Model.

by Figures 2.13. As the Mach number is increased towards the test conditions of Mach 3, the angle of the shock, expansion, and recompression waves are expected to deflect and narrow down towards the sphere body. This is depicted by the simulation in Figure 2.14

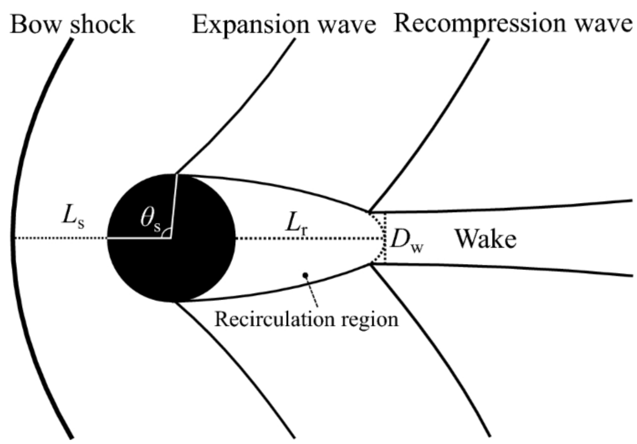


Figure 2.13: Nomenclature of Sphere Shock Structure

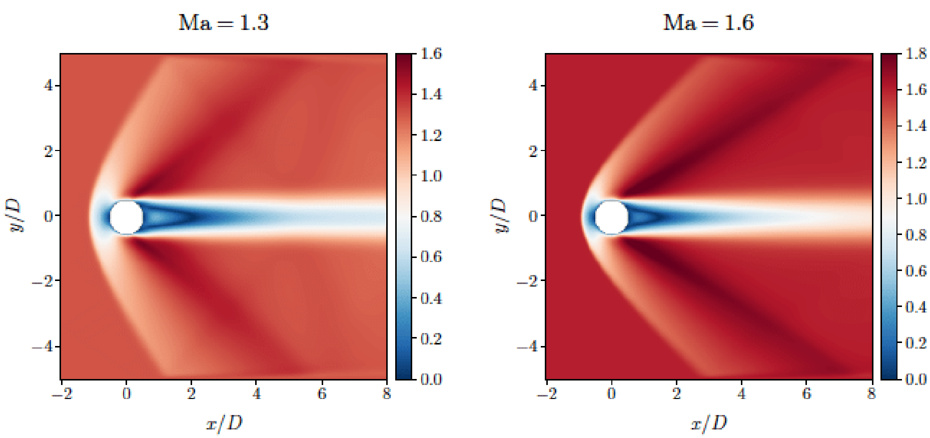


Figure 2.14: Instantaneous visualisation of the 3D supersonic flow past a sphere: Re=300 and two different Mach numbers. [13]

### 2.5.2 BOLT Model

A 2" scale-model of the BOLT test article was mounted on a sting in the tunnel test section for later tests. The model was 3-D printed out of plastic resin, and was durable enough to withstand the laser for the extent of the tests. Various aspects of the model are shown by Figure 2.15.

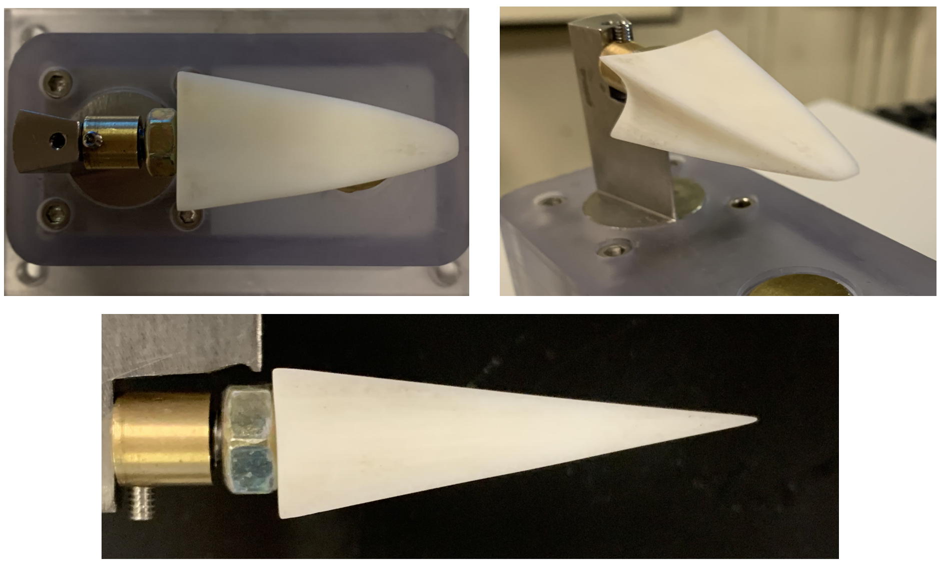

Figure 2.15: 2" Mounted BOLT Model

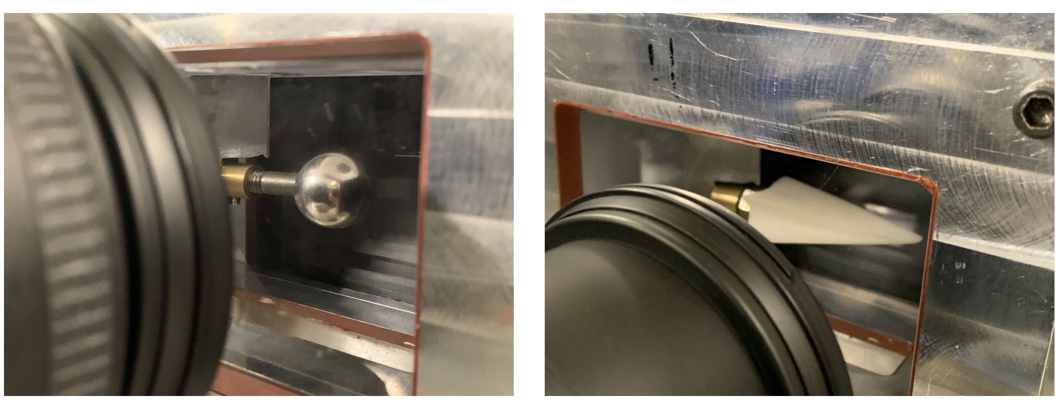

Figure 2.16: Sphere Model (left) and BOLT Model (right) mounted inside tunnel test section.

## 2.6 Imaging Equipment

Three different cameras were used in the development of the PLIF system, each with their own benefits and drawbacks. The first camera tested was the Princeton Instruments PI-MAX 2, which was suitable for identifying sheet dimensions, but not suitable for Kr-PLIF tunnel tests. The next camera tested was the PCO.Dimax HD, which was suitable for making Kr-PLIF measurements at 1000 fps. Finally, the PCO.Dicam was tested, which offered the highest signal-to-noise ratio.

In each case, an intensifier was necessary in order to increase the signal of the Kr fluorescence, which is weak by nature. The PI-Max 2 and PCO.Dicam were equipped with an internal intensifier, whereas the PCO.Dimax HD utilized an externally mounted LaVision HighSpeed IRO intensifier.

### 2.6.1 Lens and Filter

For all of the cameras, a Nikon f-mount macro lens was used with a 760 (+/- 10) nm filter. The filter has a transmission of 60%. The filter was necessary in order to reduce the noise associated with room light and residual laser reflections from the Ti-Sapphire's 810 nm beam. Even in a gated mode, the noise from these sources can be quite high relative to the signal emitted by the krypton fluorescence due to the intensifier gain.

### 2.6.2 Camera 1: Princeton Instruments PI-MAX 2

The PI-MAX 2 intensified camera system, shown by Figure 2.17 was the first one used, and was utilized during much of the sheet-forming and laser-tuning tests of this project. This camera was used previously for krypton tagging velocimetry (KTV) [17] at the 760 nm wavelength of interest here.

The PI-MAX 2 is a 16-bit 1024x1024 pixel imaging system with an internal CCD and 18 mm Gen III Extended Blue intensifier. For the Kr-PLIF experiments, the gain was set at 255 (maximum), and a 25 ms gate allowed approximately 25 fluorescence cycles to be captured per frame.


Figure 2.17: Princeton Instruments PI-MAX 2.

The PI-MAX 2 camera head houses both the internal CCD and intensifier, and is cooled by an attached fan and liquid coolant circulation system. The camera had also has an F-mount to which the Nikon macro lens was mounted. An external programmable timing generator and power supply is connected via wire to the camera. A high-speed serial link allows data to be transferred directly to the host computer during recording windows.

The camera is able to be operated in shutter or gate mode. For the Kr-PLIF experiment, the camera was set to gate mode and externally triggered by the 1 kHz laser signal.

The camera was not sensitive enough to gather an appreciable signal from single pulses, so the 25 pulse-per-frame capture was necessary. Further boosts in signal were made by averaging 10 frames (250 pulses, 250 ms) together. A major issue with the PI-MAX 2 at these settings was that the 4 Hz framerate only allowed 5-6 steady state PLIF images to be captured in each tunnel run. This would not be acceptable in a tunnel with shorter run times, such as the UMD Ludwieg Tube.

### 2.6.3 Camera 2: PCO.Dimax HD & LaVision HighSpeed IRO

The PCO.Dimax HD camera, shown by Figure 2.18 utilizes a Complementary Metal Oxide Semiconductor (CMOS) active pixel sensor in order to convert light into electrical signals. The sensor is very similar in function to a CCD. The camera is capable of capturing images at up to 2128 fps at full HD resolution (1920 x 1080 pixel). It has 12-bit dynamic range, and images are stored on-board in internal memory (36 GB maximum) as 12-bit .tif files.

In the Kr-PLIF setup, with the camera/intensifier externally gated, the operational frame-rate was identical to the pulse frequency of the laser (1 kHz = 1,000 fps).

The LaVision HighSpeed IRO, shown by Figure 2.19, is an intensified relay


Figure 2.18: PCO.Dimax HD Camera.

optic system equipped with gated high precision shutter control. It is specifically designed to be used in series with common CMOS cameras, and provides a high sensitivity peak within the visible range. The S25 photo-cathode response is near its peak at the 760 nm wavelength emitted by the krypton fluorescence, as shown by Figure 2.20.


Figure 2.19: LaVision HighSpeed IRO.

Gating times can be brought down to as short as 100 ns, which serves to minimize the noise obtained while measuring the extremely brief (20-60 ns) periods of krypton fluorescence during each laser pulse. With a max repetition rate of 2 MHz, the intensifier is well suited for triggering on the 1 kHz repetition of the laser.

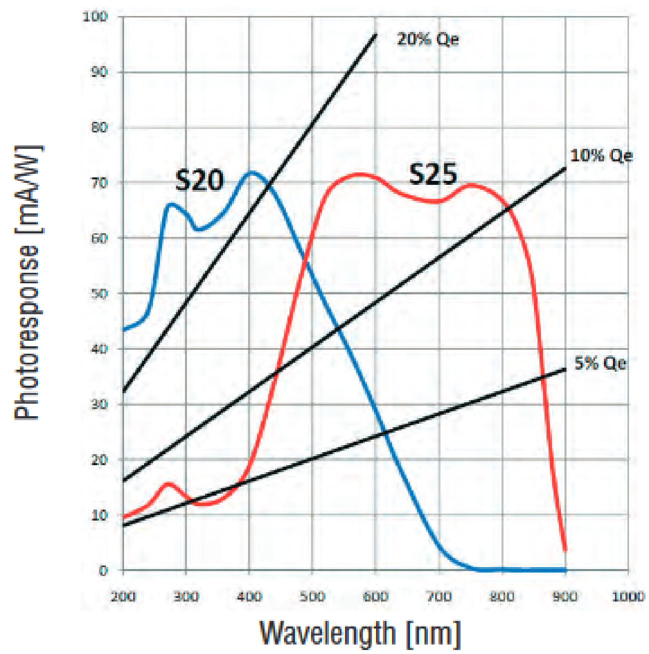


Figure 2.20: HighSpeed IRO Photcathode Response.

During the tests, the PCO.Dimax/IRO was operated with a 135 ns gate and 90 ns delay. The gain was set at 90%.

The Nikon macro lens was mounted directly to the F-mount of the LaVision HighSpeed IRO. The IRO was then mounted directly to the PCO.Dimax HD. This effectively created a single rigid body system, which was mounted to a series of rails, which allow this large system to be easily mobile between multiple different experiments. The rail system also allowed for adjustments to the camera height and viewing angle. This system is shown by Figure 2.21

### 2.6.4 Camera 3: PCO.Dicam C1 UHS

The final camera tested was the PCO.Dicam C1 UHS intensified 16 bit sCMOS camera, shown by Figure 2.22. The camera has a resolution of 1504 x 1504 pixels,

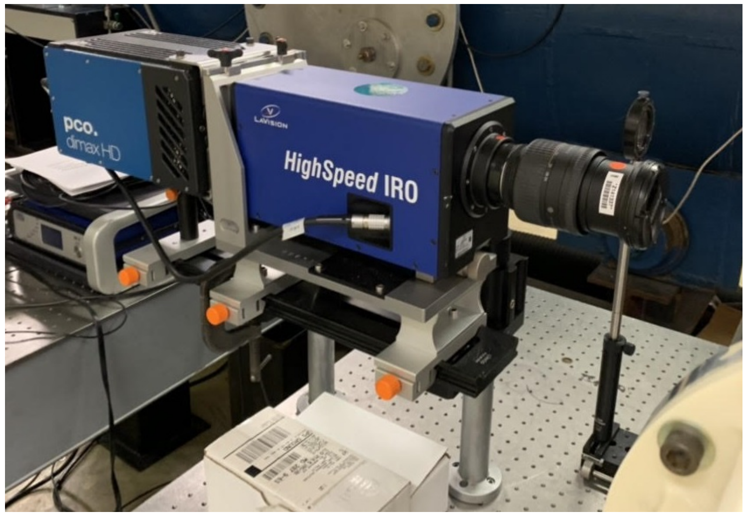


Figure 2.21: Mounted PCO.Dimax/IRO System.

and can capture images at 143 fps at full 2.3 MP resolution. Additional repetition rate above 143 fps can be achieved by lowering the resolution to view a particular region of interest. The camera has the lowest readout noise of any gated intensified camera system on the market, and can gate as short as 2.5 ns.


Figure 2.22: PCO.Dicam C1 UHS intensified CMOS camera

The internal intensifier is directly coupled to the 16 bit sCMOS sensor via an efficient tandem lens. The intensifier can utilize one of three photocathodes, each with a peak efficiency at a different wavelength, as shown by Figure 2.23. For the

760 nm application of Kr-PLIF, the GaAs photocathode was utilized.

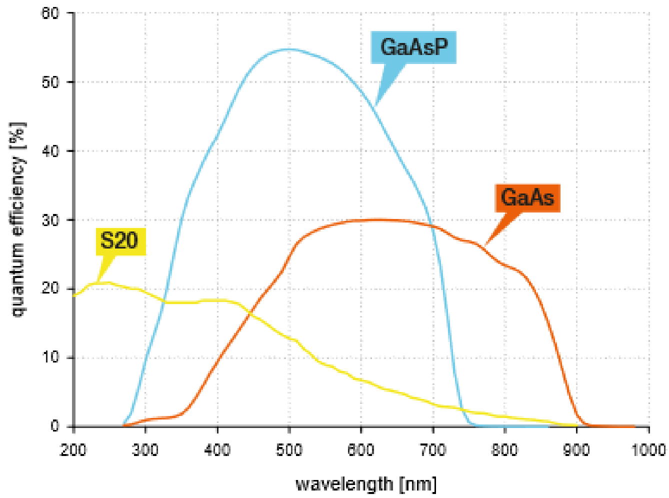


Figure 2.23: PCO.Dicam Intensifier Photocathode Quantum Efficiency

An immediate advantage of the PCO.Dicam over the PCO.Dimax/LaVision IRO is its high mobility. The PCO.Dicam is about half the length and width of the latter system, and is much more easily mounted/manipulated. This can be particularly important if the camera is to be rotated in order to image a particular surface region on a model.

## 2.7 Post-Processing Software

### 2.7.1 LaVision Davis

The LaVision Davis imaging software was used in order to process the .tif images gathered from the tunnel runs by each camera. The Davis package is a complete software solution for intelligent (laser) imaging for fluid dynamics, combustion, spray applications as well as material strain and deformation imaging.

Of particular interest to this project, the Davis software can produce calibrations to de-warp images, which allowed images to be taken of the Kr-PLIF setup in the test section from non-right angles. This is fundamental to being able to analyze the Kr-PLIF data on curved surfaces, which was a major motivation for this research.

The Davis software also allows for the intuitive construction of masking functions. In most cases, the PLIF data was time-averaged and underwent Gaussian smoothing. This was necessary in order to construct a more accurate representation of shock qualities. Additionally a mask was generated for each test setup in order to subtract background noise from the .tif images, which served to maximize the signal-to-noise ratio of the fluorescence signal. In most cases, image background subtraction increased the signal-noise-ratio by about 5-10x.

Processing of an image set for each tunnel run took anywhere between 2-15 minutes, depending on the masking functions utilized. This represents a relatively quick solution for extracting usable data following a successful test.

### 2.7.2 Density Evaluation

The main goal of PLIF is to translate a fluorescence signal into a quantifiable density measurement. This relation is again described by Equation 2.8:

$$S = C\frac{A_{21}}{A_{21} + \sigma_0 nv}n \tag{2.8}$$

where S is the fluorescence signal, n is the Kr number density, $A_{21}$ is the Einstein coefficient for the transition, $\sigma_0$ is the self-quenching cross-section, v is frequency of the emitted photon, and C is the calibration coefficient.

The density can also be found by Equation 2.11,

$$\rho = \rho_0 \frac{S}{\bar{S}_0} \tag{2.9}$$

where $\rho$ is the density at a point in the flow, $\rho_0$ is the ambient density in static air, S is the signal of fluorescence at some point in the flow, and and $S_0$ is the average signal of fluorescence in static conditions.

Alternatively, a numeric approach can be taken for processing of .bmp images of x-rows and j-columns by the following modification to Equation 2.11:

$$\rho(x,j) = \rho_0 \frac{S(x,j)}{\bar{S}_0} \tag{2.10}$$

$$\bar{S}_0 = \sum S_0(x,j) \frac{1}{N} \tag{2.11}$$

where N is the number of pixel elements contained within the bounds of (x,j).

# Chapter 3: Results

## 3.1 Overview

Each of the three cameras were evaluated with wind-tunnel tests at approximately Mach 3. During the tests, the first goal was to be able to visualize the shock with Kr-PLIF. Once the shock could be visualized, the next goal was to evaluate relative densities change within the flow as a function of the krypton fluorescence signal.

Additionally, Schlieren imaging was conducted about the models in order to establish a baseline for visualization of shock formation at Mach 3 to which the Kr-PLIF results could be referenced.

## 3.2 Schlieren Imaging

### 3.2.1 Schlieren: Sphere

40 images were first taken about the 0.5" stainless steel sphere at 100 Hz, and then time-averaged to form a single image across 0.4 seconds of flow. The resultant shock and expansion waves about the sphere are shown in Figure 3.1.

The primary shock had a standoff distance of approximately 0.04 in (1 mm).

The expansion wave began at approximately the midpoint of the sphere body. Both the shock and expansion wave had an angle of about $36^o$ relative to the x-plane of the sphere. Minor shock reflections could be seen throughout the tunnel run and are visible in the image.

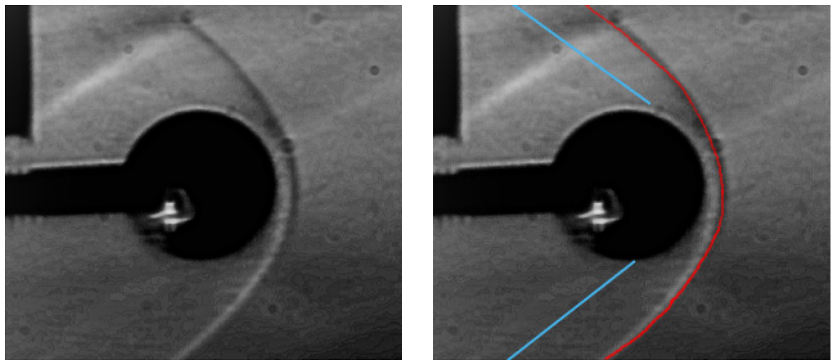

Figure 3.1: Schlieren: 0.5” Sphere at Mach 3

### 3.2.2 Schlieren: BOLT, Side Profile

Next, 50 images were taken about the 2" BOLT model at 100 Hz, and then time-averaged to form a single image across 0.5 seconds of flow. The orientation of the model was normal to the field of view (no bank/rotation), and was mounted at approximately $3^o$ AoA.

The resultant shock about the BOLT model is shown by Figure 3.2. The shock had no measurable standoff distance from the leading edge of the model. The upper-surface shock had an angle of about $27^o$ relative to the x-plane of the model. The lower-surface shock had an angle of about $25^o$ relative to the x-plane of the model. This slight difference is due to the angle-of-attack of the model, which was expected to also create a greater density buildup on the lower-surface of the model, as will be evaluated with Kr-PLIF in the sections to follow.

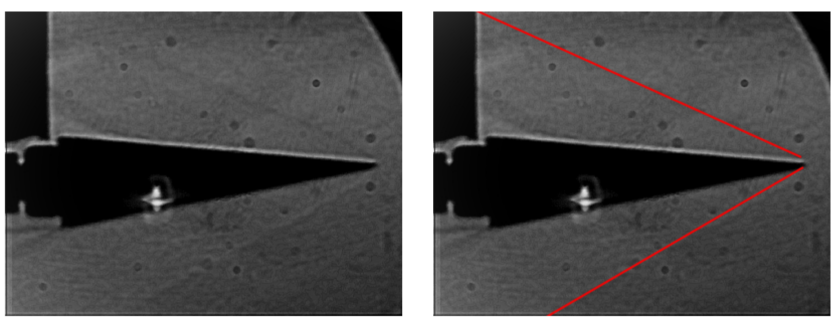

Figure 3.2: Schlieren: 2" BOLT Model at Mach 3

### 3.2.3 Schlieren: BOLT, Rotated $45^o$

Finally, 50 images were again taken about the 2" BOLT model at 100 Hz, and then time-averaged to form a single image across 0.5 seconds of flow. The orientation of the model was rotated to $45^o$ of bank, and the model was again mounted at approximately $3^o$ AoA.

The resultant shock about the BOLT model is shown by Figure 3.3. As before, the shock had no measurable standoff distance from the leading edge of the model. The upper-surface shock had an angle of about $26^o$ relative to the x-plane of the model. The lower-surface shock had an angle of about $24^o$ relative to the x-plane of the model.

As expected, it is impossible to gain any information about the shock down to the curved surface of the BOLT model using Schlieren, even with the model rotated, as the surface is entirely obscured by the through-and-through FOV requirements of Schlieren and shadowgraph methods. This test, however, did provide a reference to which the Kr-PLIF test in Section 3.5.3 could be compared.

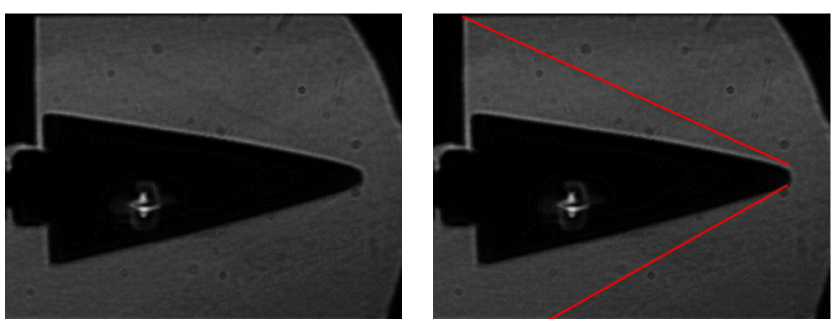

Figure 3.3: Schlieren: 2" BOLT Model (rotated $45^o$) at Mach 3

## 3.3 Kr-PLIF: PI-MAX 2 Results

The PI-MAX 2 was the first camera tested, and a wide variety of sheet combinations were evaluated, including:

- 1.0" Wide Sheet, 1-D Focused
- 1.0" Wide Sheet, 2-D Focused
- 0.5" Wide Sheet, 1-D Focused
- 0.5" Wide Sheet, 2-D Focused
- 0.5" Wide Sheet, Collimated

The most notable results of the tests are shown in the following sections. Overall, results were not consistent nor promising when using the PI-MAX 2. In order to reliably see the fluorescence, the images had to be added and averaged during capture, and in doing so, the camera could only export about 3-5 usable images for each run (approximately a 1 Hz frame rate). In the following examples, 25 images were captured and averaged per second in order to produce the following signals.

### 3.3.1 Test: PI-Max 2 with 0.25" Focused Beam

An attempt was first made to visualize the bow shock about the leading edge of the ball bearing. The 0.25" laser sheet was focused at the leading edge of the sphere, and the beam was allowed to slightly impinge the sphere geometry. Therefore, the primary region of interest is the upper half of the sphere, prior to impingement. The

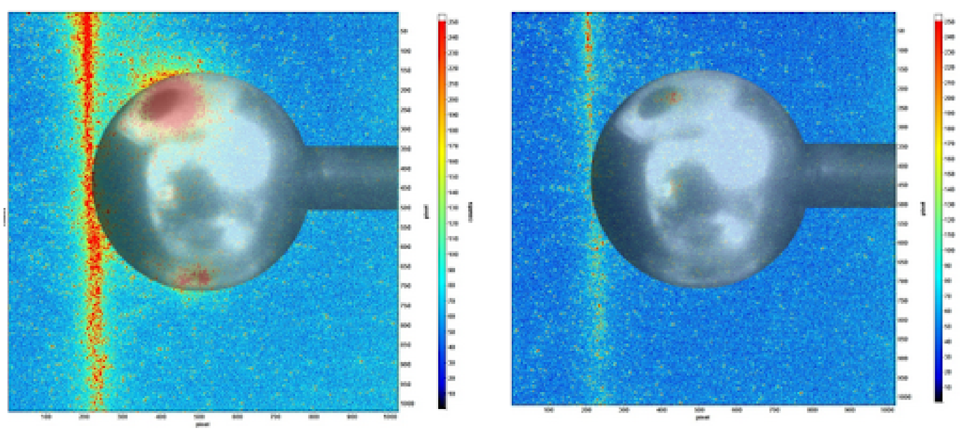

Figure 3.4: Test: PI-MAX 2 with 0.25" Focused Beam, Leading Edge. Static (left), Mach 3 (right)

PI-MAX 2 was not sensitive enough, even with averaging, to consistently capture the fluorescence signal in this setup. A visualization of the bow shock was not readily discernible.

### 3.3.2 Test: PI-MAX 2 with 0.25" Focused Beam

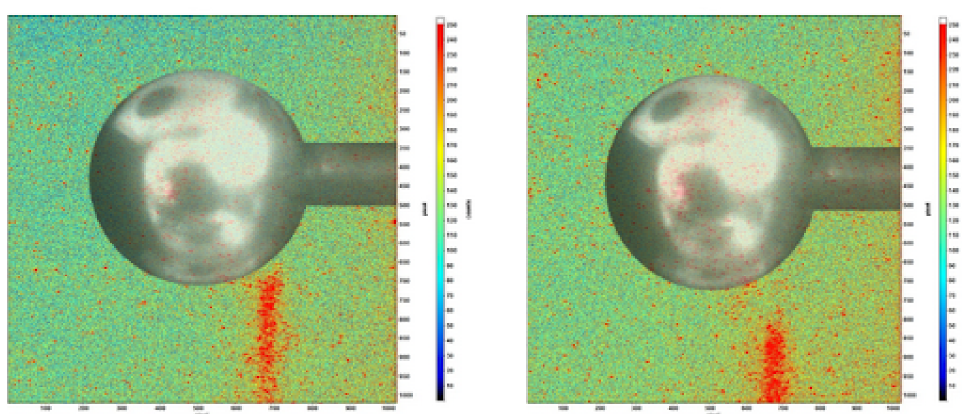

Figure 3.5: Test: PI-Max 2 with 0.25" Focused Beam, Wake Area. Static (left), Mach 3 (right)

The same 0.25" focused beam was then tested in the aft-portion of the sphere in an attempt to visualize the flow separation following the mid-body expansion wave (referred to in Figure 2.13). This effort was reasonably successful, as there was a consistent point at which the signal of the krypton fluorescence was disturbed. However, the quality of this signal was too deficient to be able to characterize this disturbance in an exact manner.

### 3.3.3 Test: PI-MAX 2 with 0.5” 1-D Focused Beam

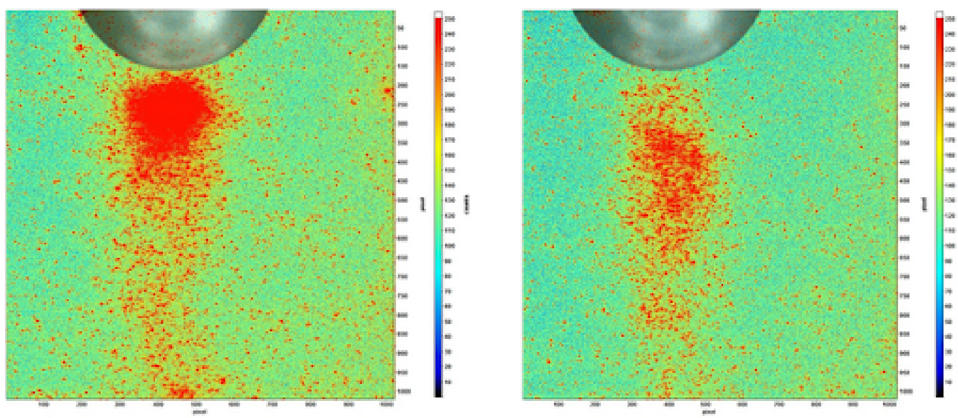

Figure 3.6: Test: PI-Max 2 with 0.5” 1-D Focused Beam, Wake Area. Static (left), Mach 3 (right)

A 0.5” 1-D focused sheet was tested order to visualize a wider region of interest along the length of the sphere body. The 250 mm cylindrical plano-convex focusing lens resulted in a usable fluoresced region of interest that was about 0.3” x 0.3”. In this test, the shock location was able to be roughly visualized, and a difference in density was observable above and below the shock. However, the observed signal was not strong or consistent enough in order to accurately assess the values of density in this region. This was the primary issue with the PI-MAX 2 across all tests.

## 3.4 Kr-PLIF: PCO.Dimax Results

### 3.4.1 Test: PCO.Dimax, Single Image, No Averaging

The PCO.Dimax 2 and LaVision IRO were tested next. Initially, a 0.25" x 0.025" collimated sheet was used. The camera gate was set to 25 ms, which allowed 25 pulses to be captured per image. The noise background was subtracted to maximize the signal-to-noise ratio. Some slight bow shock activity could be observed, as shown by Figure 3.7, and there were definable variations in fluorescence signal across the shock.

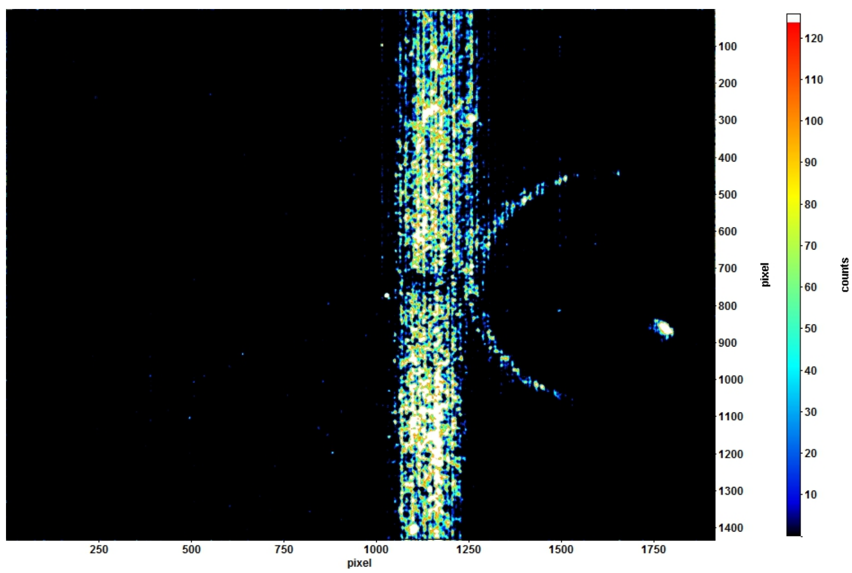


Figure 3.7: Test: PCO.Dimax, Single Image, No Averaging

### 3.4.2 Test: PCO.Dimax, Time Averaged for 250 pulses

In order to improve upon the fluorescence signal fro the previous test, a 0.25" sheet was focused down in the y-dimension. Additionally, the 25-pulse images were time-averaged across 10 images, producing time-averaged images that contained the signal representation of 250 pulses. Following the success of the first image about the leading-edge/bow shock, 4 more images were taken along the sphere geometry. All 5 images were then summed together in order to form a single, composite image about the entire test article, as shown by Figures 3.8, 3.9, and 3.10.

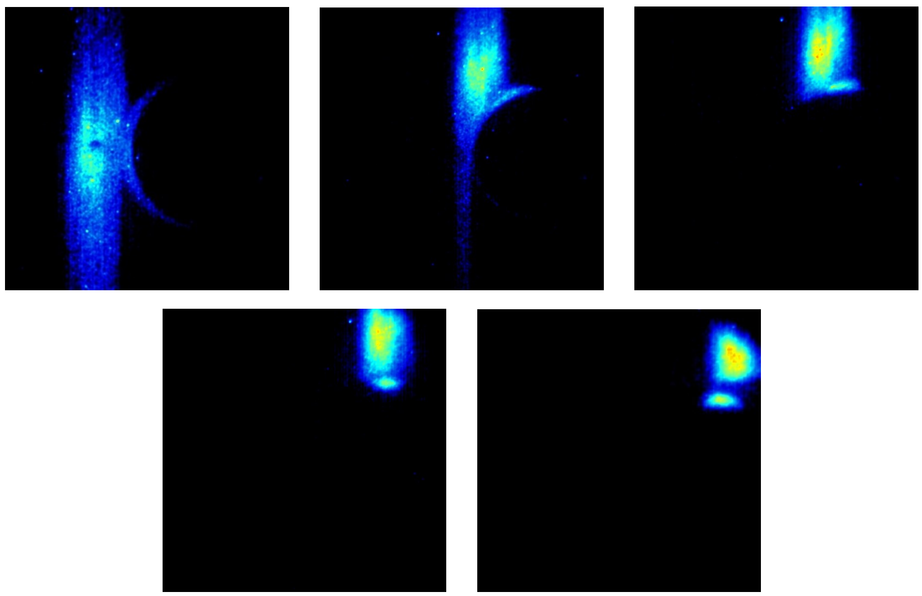

Figure 3.8: Test: PCO.Dimax, Series of Images from 5 Runs, Time Averaged for 250 pulses, 16k Resolution

From Figure 3.9, a shock and expansion zone can clearly be identified across the sphere. The fluorescence signal is significant enough in order to obtain a consistent depiction of the flow density in the fluoresced regions. Additionally, flow activity can be seen within the boundary region close to the surface of the sphere. However, the resolution of the PCO.Dimax is too low, even with a macro lens, to get a clear view of motions within the boundary layer region.

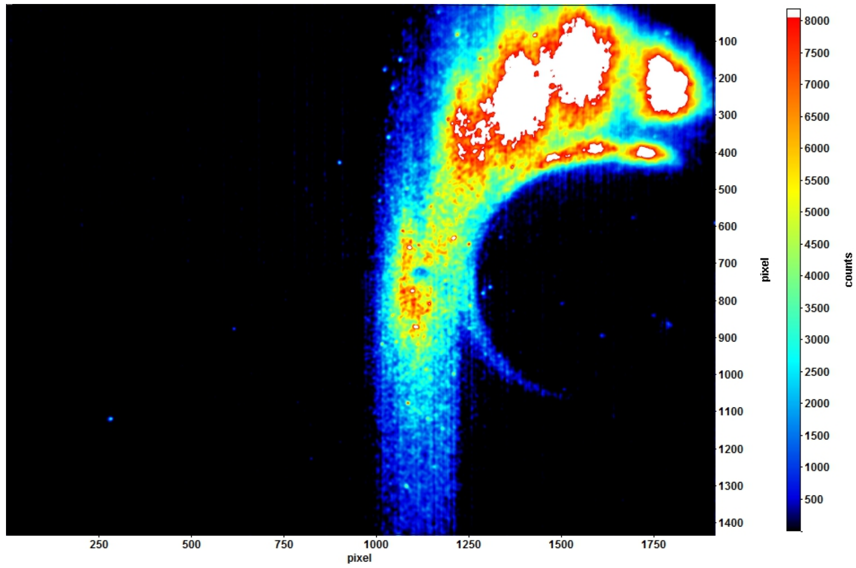


Figure 3.9: Test: PCO.Dimax, Composite Image, Time Averaged for 250 pulses, 8k Resolution

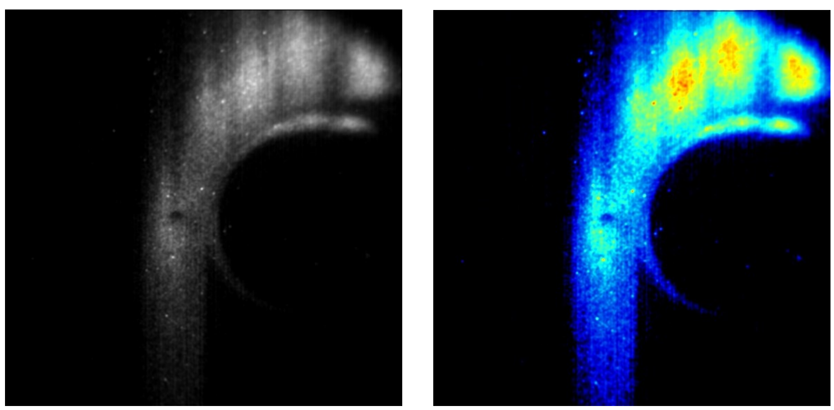

Figure 3.10: Test: PCO.Dimax, Composite Image, Time Averaged for 250 pulses, 16k Resolution. Black  White (left), False-Color (right).

## 3.5 Kr-PLIF: PCO.Dicam C1 UHS Results

### 3.5.1 Test: PCO.Dicam, Sphere, Time-Averaged for 200 pulses

The PCO.Dicam was initially tested against the sphere model with a gate of 100 ns, framerate of 200 Hz at 900 x 900 pixel resolution, no software delay, and maximum gain. The PCO.Dicam captured one laser pulse/fluorescence cycle per gate, which resulted in much lower noise that the 25 ms, 25 pulse gate utilized by the PCO.Dicam. Unlike the PCO.Dicam, the PCO.Dimax was capable of seeing adequate signal from this single pulse/gate scenario.

In post-processing, the background was removed and the signals were magnified for visibility. Five images, time-averaged across 200 individual gates, were combined to form a composite image, as shown by Figure 3.11.

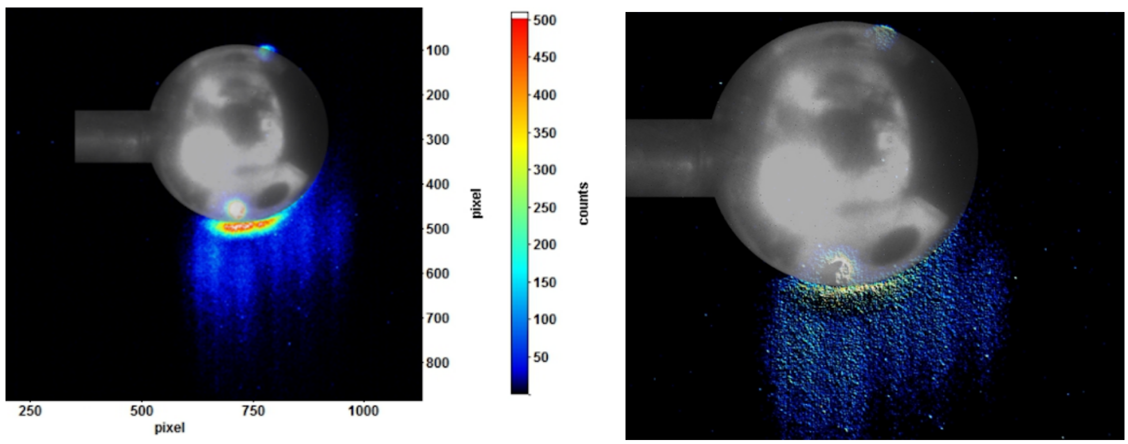


Figure 3.11: Test: PCO.Dicam, Sphere, Composite Image Time-Averaged for 200 pulses. Relative intensity map (left), Sobel-filtered image (right).

A region of high fluorescence intensity can be seen alongside the bottom of the sphere, which grows in thickness along the length of the sphere. At the edge of this region is the location of the expected primary shock (across a shock, there is a sharp rise in density). However, when overlayed with the Schlieren image for the sphere, as shown by Figure 3.12, it appeared that this region of high density does not actually delineate the shock line. One possible explanation then for this exceptionally high relative density and Kr fluorescence, is that this region is actually the boundary layer of the sphere, which is expected to grow as a function of distance across the sphere surface.

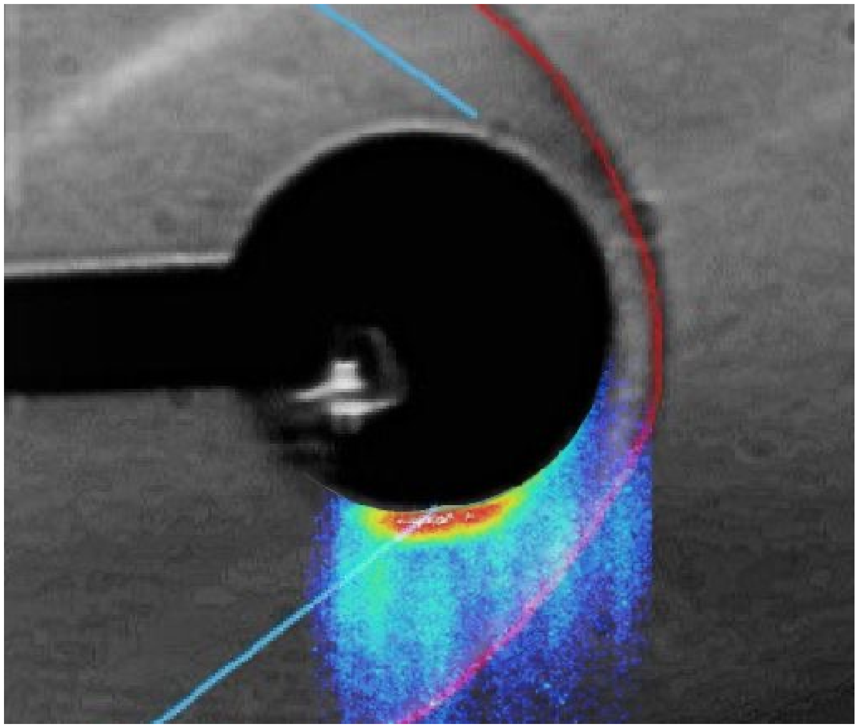

Figure 3.12: Schlieren/Kr-PLIF Overlay: Sphere

### 3.5.2 Test: PCO.Dicam, BOLT, Time-Averaged for 400 pulses

Following the success of visualizing density variation about the sphere, the BOLT model was tested next. The BOLT test was averaged for 400 images at 200 Hz (2 seconds), during the duration of steady flow in the Mach 3 tunnel. The background noise intensity was about 95 counts, and the average fluorescence signal intensity in each test was about 100-175 counts above average. This resulted in average pre-filtered intensity counts of about 195-270 counts. The results are shown by Figure 3.13 and 3.18.

A region of relative high density was observed on the underside of the leading edge. This region extends for approximately 5 mm along the BOLT model, and has a maximum thickness of about 1.5 mm (extending out from the surface). This

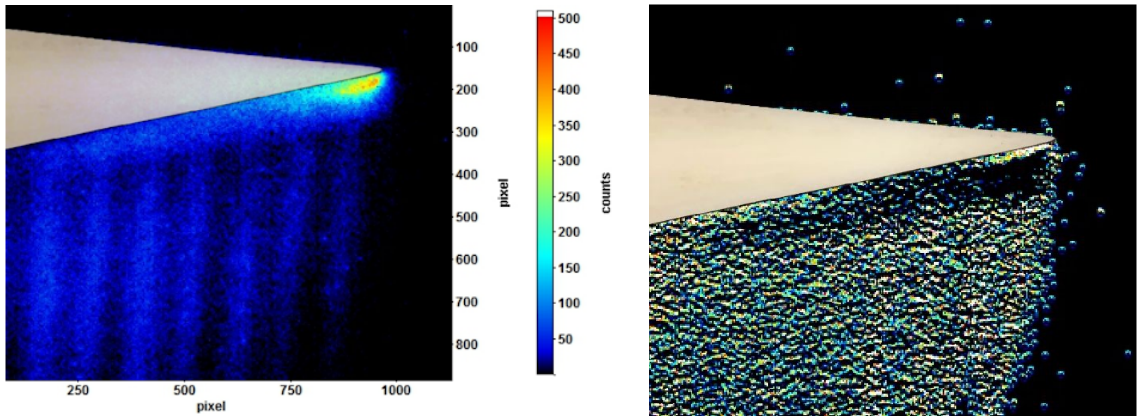


Figure 3.13: Test: PCO.Dicam, BOLT, Composite Overlayed Image Time-Averaged for 400 pulses. Relative intensity map (left), Sobel-filtered image (right).

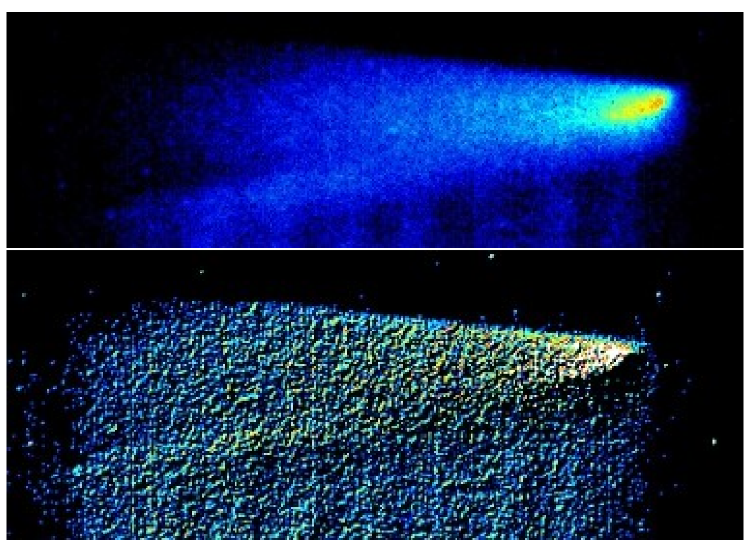

Figure 3.14: Test: PCO.Dicam, BOLT, Raw Composite Image Time-Averaged for 400 pulses. Relative Intensity Map (top) Compass Filter Edge Detection (bottom).

region of high density was likely a result of the $3^o$ AoA of the model.

There is also a region of moderate fluorescence which extends for the entire length of the laser sheet-composite along the body of the model. Because of the linear nature and relatively defined edge of this region of moderate fluorescence, it was first believed to be an indicated of the weak shock about the model. Figure 3.15 displays an overview of the Schlieren and Kr-PLIF tests in order to investigate this further.

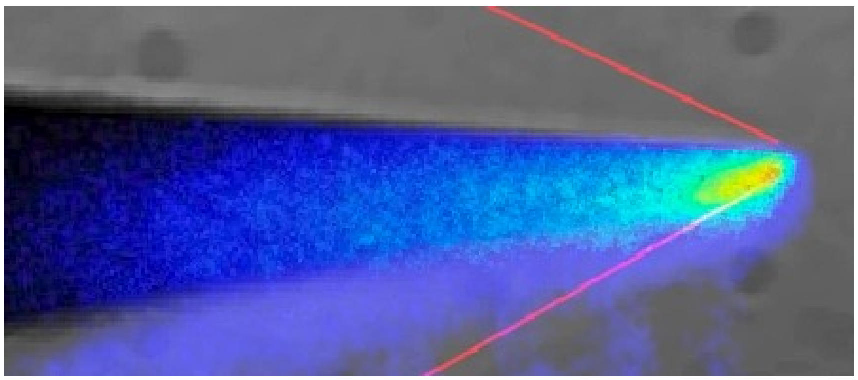

Figure 3.15: Schlieren/Kr-PLIF Overlay: BOLT Model, Normal to FOV

There was an approximately 4-$6^o$ angular distance between the edge of the region of moderate Kr fluorescence and the location of the shock observed in the Schlieren test. One possible explanation for this could be that the seeding of the gas with 5% Kr resulted in a slightly greater flow density and specific heats ratio, from what was experienced in the Schlieren test. This would cause a change in shock angle (by about $2^o$), and could *partially* explain the difference in shock geometries as directly observed in the Schlieren test and *inferred* by the Kr-PLIF test. However, the signal of the Kr-PLIF was still too weak to say with absolute certainty that this explanation is accurate.

### 3.5.3 Test: PCO.Dicam, BOLT rotated by $45^o$, Time-Averaged for 400 pulses

In this test, the BOLT model was rotated to $45^o$ of bank, such that the camera had a view of the laser sheet all the way down to the curved surface, which was obscured in the previous test and in Schlieren imaging. The results are shown by Figures 3.16. Prior to filtering, the fluorescence signal had an average intensity of about 100-200 counts above background in each laser pulse. With a background of about 95 counts, this resulted in fluorescence intensities between 200 and 300 counts. In comparison to the previous test, where the BOLT model was not rotated, there was significantly more reflection that had to be taken into account during post-processing. This is due to the angle of the model (which reflected light towards the camera), as well as the material (the white plastic-resin used to 3D-print the model is not light-absorbent).

There was a slight growth in the fluoresced region that can be observed. The region of highest intensity grows from 0 mm to about 2 mm across the span of about 20 mm. This may be due to the shock about the BOLT model, which results in a region of higher density between the shock and the model surface. Another possible explanation for this is that it is an indication of boundary layer growth along the surface of the model. However, this is unlikely given the thickness of the layer relative to its position near the leading edge of the model. This is something that can be investigated further as more computational simulations and boundary layer specific tests are performed by the BOLT program. The edge of this zone can

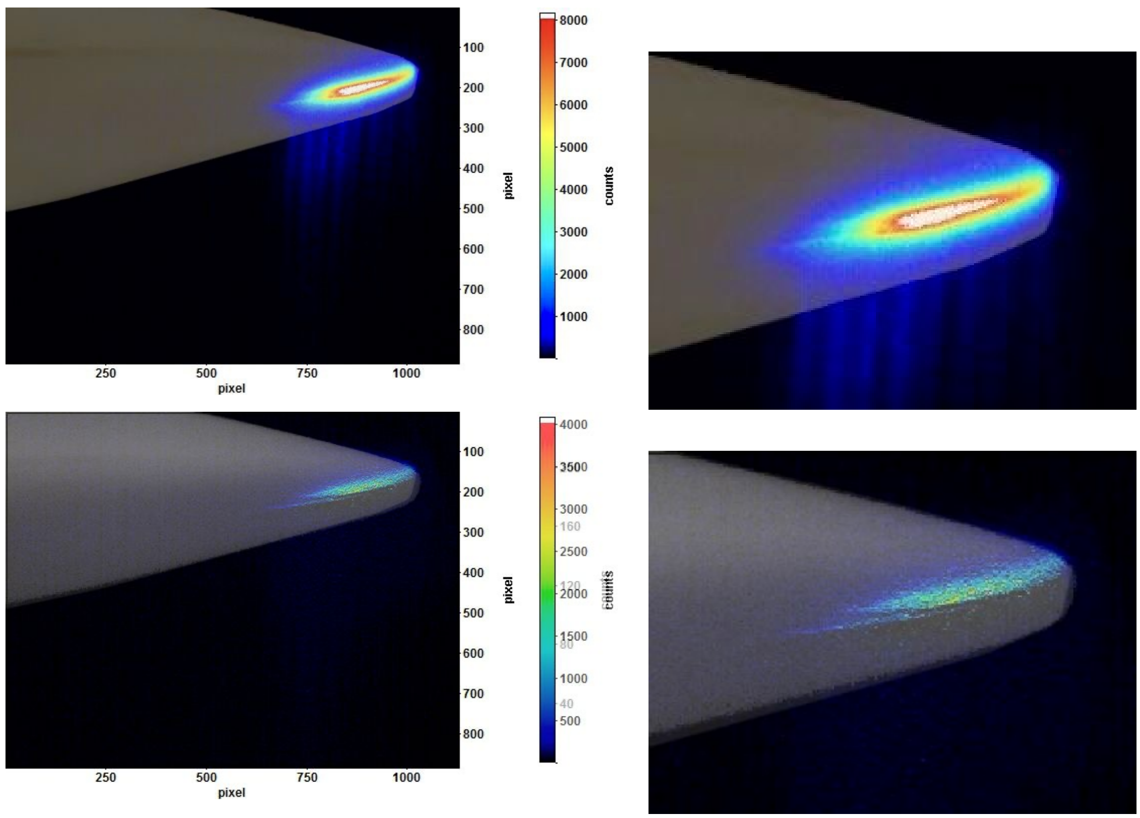


Figure 3.16: Test: PCO.Dicam, BOLT rotated by $45^o$, Composite Overlayed Image Time-Averaged for 400 pulses.Relative intensity map (left), Sobel-filtered image (right).

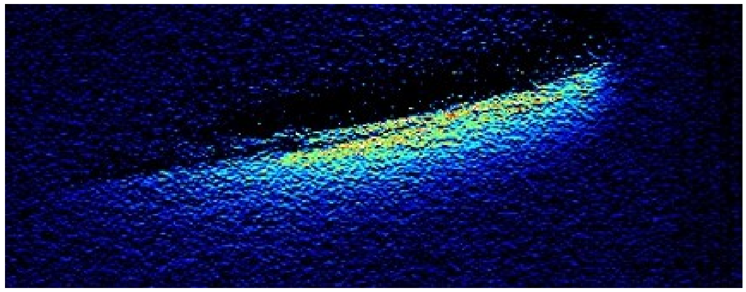

Figure 3.17: Test: PCO.Dicam, BOLT rotated by $45^o$, Raw Composite Image Time-Averaged for 400 pulses. Compass Filter Edge Detection.

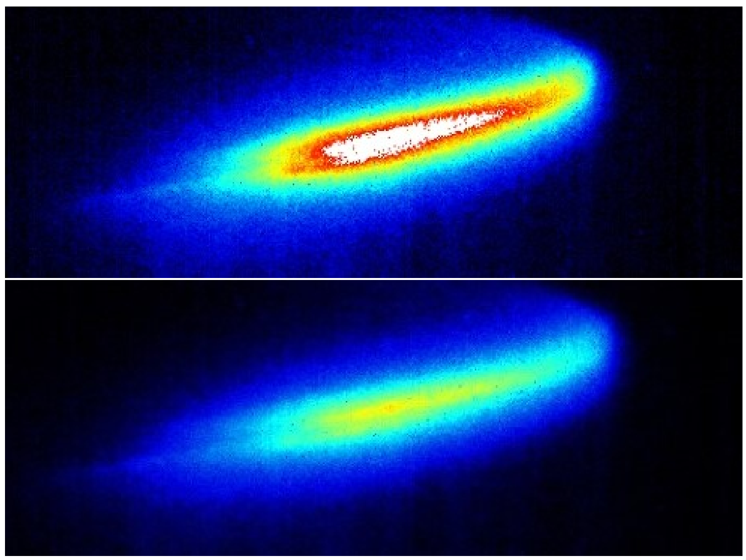

Figure 3.18: Test: PCO.Dicam, BOLT rotated by $45^o$, Raw Composite Image Time-Averaged for 400 pulses. 8k Resolution (top), 16k Resolution (bottom).

be more clearly depicted with a compass filter, as shown by Figure 3.17.

This is a result that cannot be visualized with Schlieran imaging due to the geometric constraints of the curved body surface, which was a primary motivation for the development of Kr-PLIF. Figure 3.19 displays the region of fluorescence observed, relative to what was observable by the Schlieren image for the rotated BOLT model.

The fluoresced region, particularly the region of relatively high fluorescence, lies almost entirely out of the observable region for Schlieren imaging. While there

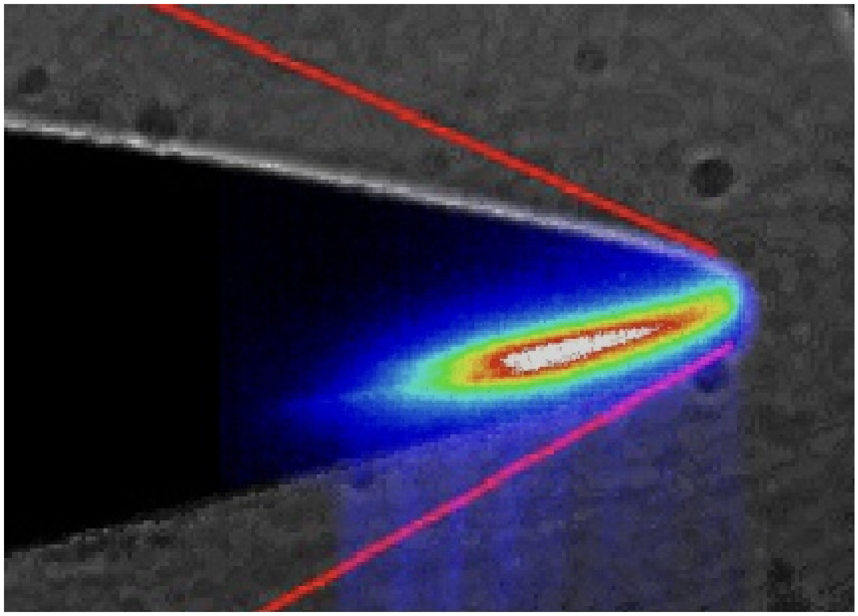

Figure 3.19: Schlieren/Kr-PLIF Overlay: BOLT, Rotated $45^o$

was speculation as to the the cause of the fluorescence variation in this region, Kr-PLIF was successful in providing information about a region that was previously unobservable by most other non-intrusive flow visualization methods.

# Chapter 4: Conclusions and Future Work

## 4.1 Conclusions

Three cameras and several laser sheet sizes were evaluating for Kr-PLIF using 5% Kr/95% $N_2$. Measurements were taken about a 0.5" metal sphere, and a 2" model of the BOLT test article. It was found that the best Kr-PLIF results came from using the PCO.Dicam C1 UHS intensified camera with a 760 +/- 10 nm filter and a 0.225" long, focused sheet. The focused sheet provided a 0.225" x 0.3" region of usable fluorescence. Signal intensities varied between an average of 200-300 counts, above a background of an average of 95 counts. Density variations across a shock were able to be visualized, and regions of relatively high density were identified. The primary shock itself was also able to be partially visualized. Composite images were formed from 4-5 tunnel runs for each test article condition and compared to Schlieren images about the same test articles. The Kr-PLIF was able to visualize a density variation and possible shock formation on the concave surface of the BOLT model which was inaccessible to Schlieren imaging. However, more signal is needed to clearly delineate the shock and obtain numerical results for flow density.

## 4.2 Future Work

There is much work to be done towards improving the Kr-PLIF method if it is to be a viable form of visualizing shocks and density fluctuations about curved surfaces in hypersonic conditions in the future. For the near term, the most impactful improvement can be found in the increasing of laser power. The fluorescence signal scales exponentially with laser power, so as femtosecond laser power is increased, the quality of results should increase accordingly. Another improvement can be made by increasing the concentration of kyrpton seeded to the flow. However, this is limited by the needs of the experiment at hand, as the original flow behavior changes as more krypton is added, and hypersonic flows may be limited to 1-5% Kr. However, this can be overcome in certain applications through the use of localized seeding of high concentration krypton gas from the target model itself. This is one possibility for the BOLT program moving forward in the UMD Ludwieg Tube. Lastly, with the proper optics, thinner sheets can be made, which can allow for greater power densities and therefore a greater fluorescence signal or larger max-allowable sheet size. Based on the results of these tests, the PCO.Dicam C1 UHS series camera is the most suitable for Kr-PLIF due to its very high signal-to-noise ratio and moderate framerate.

With the necessary improvements made in order to increase signal, Kr-PLIF may become a possible near-future tool to supplement Schlieren imaging for complex geometries in high speed flows. It is unlikely, however, for Kr-PLIF to fully replace Schlieren imaging in cases where Schlieren can be used to observe the entire region of interest. A major limitation in all cases moving forward is the scale of PLIF observations. Typical sheet sizes are on the scale of fractions of an inch, and so full coverage of a large scale model is not currently realistic. However, the small sheet sizes of PLIF may be reasonably used in the near future to visualize features like specific points of boundary layer transition, or behavior within corners/joints.

# Bibliography


[1] L.E. Dogariu, A. Dogariu, R. Miles, M.S. Smith, E.C. Marineau *Femtosecond Laser Electronic Excitation Tagging Velocimetry in a Large-Scale Hypersonic Facility* (AIAA, Volume 57, Number 11. November 2019).

[2] B. Wheaton, D. Berridge, T. Wolf, R. Stevens *Boundary Layer Transition (BOLT) Flight Experiment Overview* (Fluid Dynamics Conference. 2018).

[3] I. Grant, *Particle Image Velocimetry: A Review* (Proceesings of the Insitution of Mechanical Engineers, Part C: Journal of Mechanical Engineering Science. Volume 211, Issue 1, January 1997).

[4] P.M. Danehy, S. O'Byrne, A.D. Cutler, C.G. Rodriguez. *Coherent Anti-Stokes Raman Scattering (CARS) as a Probe for Supersonic Hydrogen-Fuel/Air Mixing* (JANNAF APS/CS/PSHS/MSS Joint Meeting, Colorado Springs, CO, December 1-5, 2003).

[5] P.Z. Ejgierd, P.M. Lata. *Krypton Oxides Under Pressure* (Scientific Reports. Article 18938. 2016).

[6] P.M. Danehy, J.A. Wilkes, D.W. Alderfer, S.B. Jones, A.W. Robbins. *Planar laser-induced fluorescence (PLIF) investigation of hypersonic flowfields in a Mach 10 wind tunnel (invited)* (Heat, Flow and Combustion Diagnostics. NASA Langley Research Center, Hampton, VA. 2012).

[7] L. Yang, W. Weng, Y. Zhu, Y. He, Z. Wang, Z. Li. *Investigation of Dilution Effect on $CH_4$/Air Premixed Turbulent Flame Using OH and $CH_2O$ Planar Laser-Induced Fluorescence* (Engineering Fluid Dynamics, 12(2), 325. 2020).

[8] J. Brooks. *Development and Application of Mach 10 PIV in a Large Scale Wind Tunnel* (University of Maryland, College Park, MD. 2018).

[9] N.L.D. Bachir, A. Belasri, P.H. Guillot, B. Caillier. *Radiative Emissions in Visible–IR of Krypton Excilamp: Experimental and Theoretical Interpretations* (Plasma Chemistry and Plasma Processing. 2019).

[10] A. Mazumdar. *Principles and Techniques of Schlieren Imaging Systems* (Columbia University. 2013).

[11] S.W. Grib, P.S. Hsu, H.U. Stauffer, C.D. Carter, S.Roy. *Comparison of femtosecond and nanosecond two-photon-absorption laser-induced fluorescence of krypton*. (Applied Optics Vol. 58, Issue 27, pp. 7621-7627. 2019).

[12] S.W. Grib, P.S.Hsu, N. Jiang, J.J. Felver, S.A. Schumaker, C.D. Carter, S. Roy. *100 kHz krypton planar laser-induced fluorescence imaging* (Optics Letters 45(14). 2020).

[13] J. Latt, C. Coreixas, J. Beny, A. Parmigiani. *Efficient supersonic flow simulations using lattice Boltzmann methods based on numerical equilibria* (Royal Society. Mathematical, Physical, and Engineering Sciences. 2020).

[14] P. Velpula, D. Kramer, B. Rus *Femtosecond Laser-Induced Damage Characterization of Multilayer Dielectric Coatings* (Institute of Physics of the Czeck Academy of Sciences. 2020).

[15] Y. Liao, Y. Cheng *Femtosecond Laser 3D Fabrication in Porous Glass for Micro- and Nanofluidic Applications* (Shanghai Insitute of Optics and Fine Mechanics. 2014).

[16] P.N. Butcher and D.N. Cotter, *The Elements of Nonlinear Optics* (Cambridge University Press, Cambridge, UK, 1990).

[17] D. Zahradka, N.J. Parziale, M.S. Smith, E.C. Marineau. *Krypton Tagging Velocimetry (KTV) in Supersonic Turbulent Boundary Layers* (AIAA SciTech Forum. San Diego. 2016).

[18] H.Y. Shen, W.X. Lin, R.R. Zeng. *Second-harmonic generation and sum-frequency mixing of double-wavelength Nd:YALO3 laser to 413.7-nm violet coherent radiation in LiIO3 crystal* (Journal of Applied Physics. Volume 72, Issue 9. 1998).

[19] D. Shekhtman, N. Parziale, M.A. Mustafa. *Excitation Line Optimization for Krypton Tagging Velocimetry and Planar Laser-Induced Fluorescence in 200-220 nm Range* (AIAA 2021-1300).